Lehrstuhl für THERMODYNAMIK

SEMESTERARBEIT

Simulation of the gas flow distribution at the intake of a high temperature sensible heat storage

Autor:
Bruno Ams
Matrikel-No:
2879192

Betreuer:
Dr.-Ing. Abdel Hakim Hassabou
Dr.-Ing. Markus Spinnler

21. May 2012

Lehrstuhl für Thermodynamik
Prof. Dr.-Ing. Thomas Sattelmayer
Prof. Wolfgang Polifke, Ph.D.(CCNY)

Abstract

High temperature thermal storage in rock beds using air as a heat transfer medium was repeatedly proposed for large solar power plants and other applications which can store large amounts of energy. The efficiency of these thermal storages is influenced by several parameters for the different operating states. One instance of this aspect is that the flow distribution during the charging of the storage directly affects the pressure drop which is the main attrition at this operating state.

The subject of investigation in this study is the uniform distribution of flow as a function of various geometrical parameters during the charging process. As there are no existing plants with the dimensions which should be investigated, CFD models are the only possibility to study the ongoing processes. For this reason the design and physical limits for each parameter were especially established for the context of this study. Based on this data, a large amount of simulations were done by varying the parameters within these limits to cover the resulting parameter field. Afterwards the results of the simulations made it possible to identify trends and the most influencing geometry parameters. In conclusion, it can be affirmed that the flow distribution depends more on the geometry parameters of the flow distributor than on the flow conditions at the inlet of the heat storage.

In a second step a model consisting of two dimensionless parameters is introduced and verified which enables one to compare the different storage geometries and to achieve a more global view on the estimated survey area. This approach offers the feasibility to identify local extremes which should be avoided during a dimensioning process. Therefore some design instructions, which are able to increase the efficiency of future heat storage developments, could be implemented.

Index of Contents

List of Figures

1 Introduction

The present thesis analyzes the flow distribution of sensible thermal heat storage in rock beds using air as a heat transfer medium. This kind of storage system was repeatedly proposed for large solar power plants and other applications which can store large amounts of energy.
As these systems are in a stadium of research, there are no existing thermal storages with the dimensions which should be analyzed in this thesis. Therefore only simulation data can be presented and there is no possibility to verify the generated results in a foreseeable future. Nevertheless sensible heat storages are the most developed thermal storage technology. There are already existing test plants and the commercial launch of this technology is expected in the next years.
During the introduction, first the motivation and problem definition of this work are explained. Subsequently, the structure of the work is outlined and an insight into the underlying technologies is given.

1.1 Motivation

There is a broad consensus that the warming of the climate system is unequivocal, and scientists are more than 90% certain that most of it is caused by increasing concentrations of greenhouse gases produced by human activities such as deforestation and the burning of fossil fuels. These findings are recognized by the national science academies of all major industrialized nations. [21]
In order to reduce the emission of greenhouse gases technologies should be investigated and developed which are able to produce energy without these emissions. One possible solution is the use of regenerative produced energy, especially solar power, that can solve the problem because it is 1000 times more available than demanded. [20] In order to tap this huge potential, solar power plants like parabolic trough, tower or dish systems are necessary.
As it will be described later in more detail, sensible heat storages have many application areas which are able to reduce the emission of green house gases. On the one hand they can be applied as a solar power plant component. In this case they store large amounts of solar produced heat and offer the possibility of constant energy production without co-firing with fossil fuels. Moreover thermal storages for solar power plants are key elements to improve the operational and revenue situation of the power plant. [30]

On the other hand they can be used to optimize the compressed air storage. So sensible heat storages are used to increase the efficiency of storing regenerative generated power. As the production of regenerative energy sometimes exceeds demand, such storage technology is heavily demanded, but at the moment the efficiencies of gas compressor storages are too low for an extensive utilization. That is why it is necessary to concentrate efforts in the research of this technology.

1.2 Flow distribution in packed beds

The aim of this study is to develop a contribution to the design of the flow path in such a storage. The subject of investigation in this study is the uniform distribution of flow as a function of various geometrical parameters. For this reason CFD calculations for the inlet area of such a storage should be performed.
In order to achieve this goal, some subtasks are necessary. First there has to be set up a matching mesh for calculating the geometrical requirements. Secondly, the calculation of the hot gas flow must be processed and the requirements for the uniform flow distribution examined. In the third step the geometry parameters are varied to derive design rules for the inlet area of thermal storages.
The parameters which can influence the flow distribution are the porosity of the packed bed and the diameter of the particles in it as well as the air flow velocity, the mass flow rate, the dimensions of the storage tank and the diffuser geometry.
As the flow distribution directly affects the pressure drop it contributes to the storage's efficiency because the pressure drop is one of the biggest losses in a sensible heat storage. A good flow distribution leads to lower pressure drop and increases the efficiency of the whole system.
Besides the flow distribution is also important for an optimal utilization of the heat storage because the thermal conduction in the storage material is low. Therefore it is possible that regions in a badly charged storage do not reach their possible maximal temperature. This could lead to large attrition during the discharging process.
For this reason it is worth investigating the physical principles and phenomena happening in the storage to increase the efficiency of this technology.

2 State of the art

First a basic overview concerning the different kinds of thermal storages is presented. Questions about the necessity, applications and the advantages of the different types of heat storages are discussed in this chapter.

2.1 Energy storage

Energy storage is the storing of some form of energy that can be drawn upon at a later time to perform some useful operation. A device that stores energy is sometimes called an accumulator especially if it saves electric energy. All forms of energy are either potential energy (e.g. chemical or gravitational), kinetic energy, electrical energy or thermal energy. All these forms of energy can be stored with an appropriate method, system or technology. That means that every form of energy has itself an accumulator. As Figure 2-1 illustrates, a large variety of energy storage systems are under development [6]. Thermal energy storage (TES) will be discussed in this document as an introduction to the main topic of this thesis.

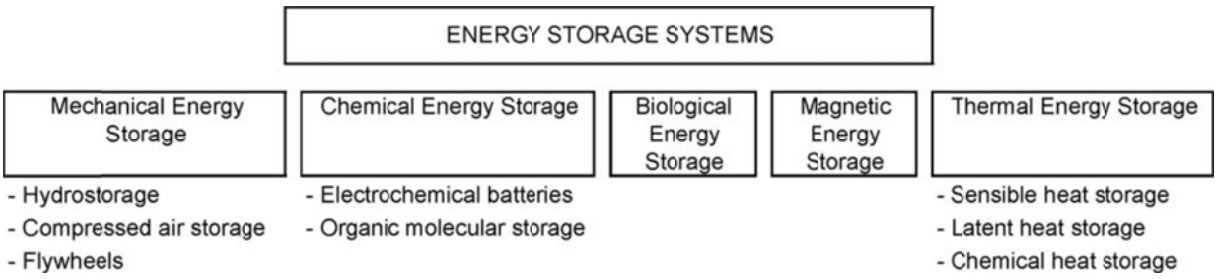

Figure 2-1: Overview Energy Storages [13]

Like in every engineering process, requirements and possibilities have to be compared and the best solution for the special case has to be found. Most of the arguments for the decision for an energy storage system are affected by cost-effectiveness, but from the technical point of view, the most important requirements are: high energy density in the storage material (storage capacity); good heat transfer between heat transfer fluid (HTF) and storage medium (efficiency); mechanical and chemical stability of storage material (must support several charging/discharging cycles); compatibility between HTF, heat exchanger and/or storage medium (safety); complete reversibility of a number of charging/ discharging cycles (lifetime); low thermal losses; and ease of adjustment control.

And finally, the most important design criteria from the point of view of technology are: operation strategy; maximum load; nominal temperature and specific enthalpy drop in load; and integration into the power plant. All these criteria have to be considered when deciding on the type and design of thermal storage. [13]

2.2 Storage media

The possibilities of thermal energy storage are manifold. As can it be seen in Figure 2-2, thermal energy can be stored thermally or chemically by means of different methods and techniques.

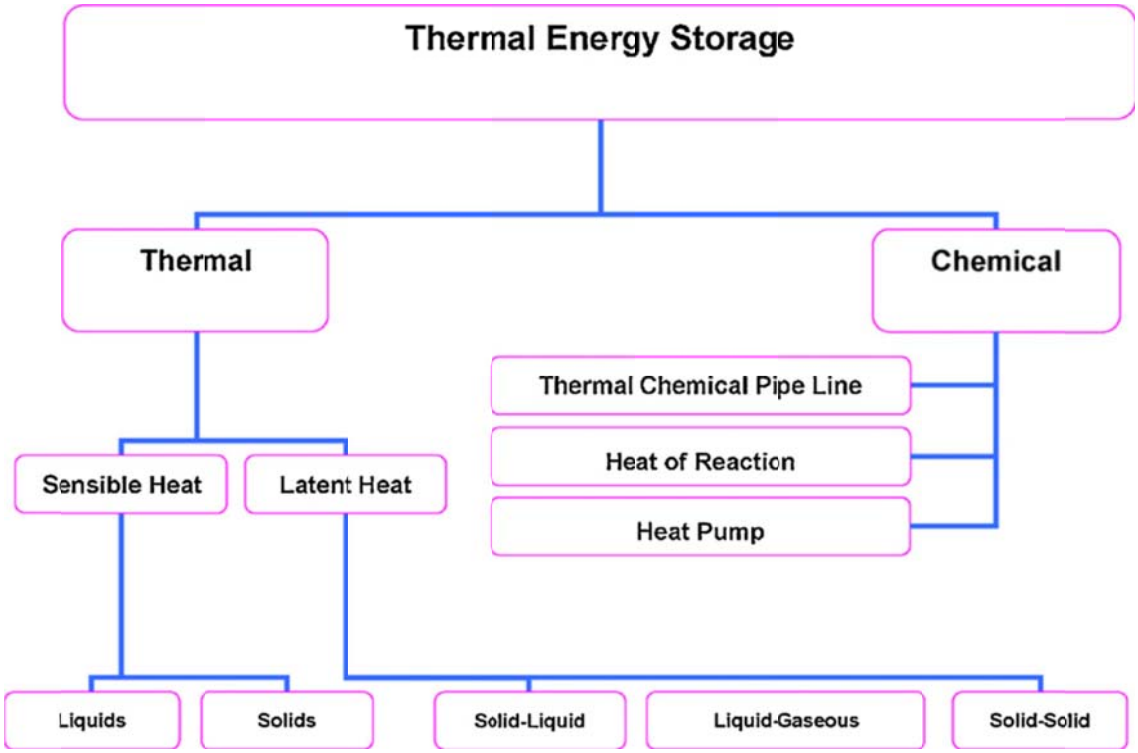

Figure 2-2: forms of thermal energy storage [35]

2.2.1 Sensible heat

The simplest possibility according to which thermal energy can be stored is to increase the internal energy of a storage material by heating it up and to conserve the sensible heat. The amount of sensible heat which a material can store is specified with the following equation:

$$Q = \rho \cdot c_p \cdot V \cdot \Delta T \qquad \text{eq. 2-1}$$

Q is the amount of energy stored in the material [J], ρ is the density of the solid [kg/m³], c_p is called specific heat capacity [J/kg·K], V is the volume of the storage material [m³] and ΔT the temperature range of the operation [°C].

A sensible thermal energy storage system consists of a tank, storage material and inlet/outlet devices like pumps and diffusers. The tank has two requirements to fulfill: It must contain the storage material and prevent the loss of the stored thermal energy. That is the reason why the tanks need a thick insulation to conserve the heat inside them.

The storage material can be either liquid or solid. When solid media is used, a fluid is needed to exchange the heat. Solid media like stones or ceramic are normally used in packed beds, but it is also possible to use bricks with drilled holes which are stacked into the tank, small spheres, cinder blocks or concrete. The decision for the use of a material depends on the considered temperature range and effects on the design of the whole storage system. For example, materials for Thermal Energy Storage (TES) application must be inexpensive and must have a good heat transfer coefficient. The heat transfer coefficient determines the rate at which the heat can be released and extracted in and from the storage. So a high surface to volume quotient and a high thermal diffusivity are desirable.

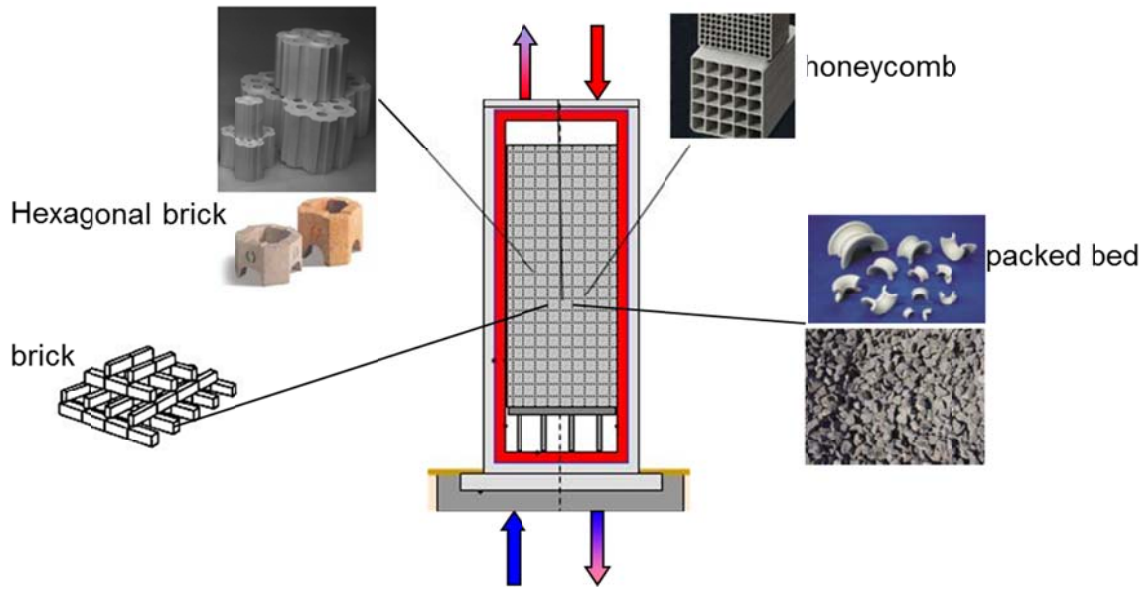

Figure 2-3: examples for sensible heat storage materials

Figure 2-3: shows the different possibilities for material selection for the storage tank of high temperature regenerators. The materials are able to resist and store very high

temperatures (up to 1300°C), which makes these systems interesting for high temperature storage. Packed beds of rocks are also simple in design and relatively inexpensive because the storage materials are basalts or other natural stone debris which is generated in stone pits as a waste product. Direct contact between the solid storage media and a heat transfer fluid is necessary to minimize the cost of heat exchange in a solid storage medium. The use of stones for thermal storage provides advantages such as the fact that rocks are non-toxic and non-flammable, rocks are inexpensive and rocks act both as heat transfer surface and storage medium. The heat transfer between air and a rock bed is good, due to large heat transfer area, low effective heat conductance of the rock pile and small area of contact between the rocks. These factors contribute to reveal the advantage of low heat losses from the pile. [17]

Hasnain [18] reported that solid materials such as rocks, metals, concrete, sand and brick can be used for low as well as high temperature heat storage. The pebble beds or rocks are generally used as storage material because of their low cost. Typically the size of rocks used varies from 1 cm to 5 cm.

Coutier and Farber [4] mentioned that packed bed generally represents the most suitable energy storage unit for air based solar power plants, because the charging process uses air as the heat transfer fluid, which makes this system particularly suitable for this type of power plants. So the heat transfer fluid can be heated up and directly pumped into the storage without any loss by cycling the heat exchanger.

On the other hand, this storage design leads to some problems. One of them is that, as the only usable potential gradient is the sensible heat, the energy density is the lowest of all presented concepts. Energy densities for a concrete-based thermal storage system have been estimated at 22 kWh/m³, resulting in 50 000 m³ sized storage for a 50MW parabolic trough power plant with 1100 MWh_{th} storage capacity. [25] Sensible heat storages must utilize a much bigger volume and heavier insulation than other concepts using phase-change materials or chemical reactions. Other tanks containing phase-change materials or molten salt also need a heavy insulation, but the temperature gradient relative to the environment is not as high (as it is in sensible heat storages). So the most expensive parts of sensible heat storages are the highly isolated tanks, especially when the tanks are designed for pressurized charging, because in any case they have to allocate a big volume.

Another disadvantage of sensible heat storages using air as processing fluid is the low thermal conductivity of the heat exchange fluid compared to other fluids like thermo-oil, sodium or molten salt. This leads to high mass flow rates which require larger, more expensive pumps and thicker pipes.

2.2.2 Latent heat

Latent heat storage systems are able to utilize the same system design as concrete or castable ceramics TES system, but with the advantage of small temperature differences between charging and discharging and higher energy densities. In the most applied pilot latent storage systems the phase change solid-liquid is used.
But PCMs latent heat storage can be achieved through solid–solid, solid–liquid, solid–gas and liquid–gas phase change. Liquid–gas transitions do have a higher heat of transformation than solid–liquid transitions but this phase changes are not practical for use as thermal storage due to the large volumes or high pressures required to store the materials when in their gas phase. Solid–solid phase changes are typically very slow and have a rather low heat of transformation.
Initially, the solid–liquid PCMs behave like sensible heat storage materials; their temperature rises as they absorb heat. Unlike conventional sensible heat storage, however, when PCMs reach the temperature at which they change phase (their melting temperature) they absorb large amounts of heat at an almost constant temperature. The PCM continues to absorb heat without a significant rise in temperature until all the material is transformed to the liquid phase. When the ambient temperature around a liquid material falls, the PCM solidifies, releasing its stored latent heat. A large number of PCMs are available in any required temperature range from −100°C up to 885°C. They store 5 to 14 times more heat per unit volume than conventional storage materials such as water, masonry or rock. [23]
In face of this benefits, PCM thermal energy storage systems are not as technical mature as sensible heat storages. The reason can be found in the low thermal conductivity resulting in a low charging and discharging rate. [7] Another problem of phase change materials are solid deposits on the heat transfer surface which develop inevitably during the discharging process if no counteractive measures are taken. Furthermore the heat transfer design and media selection are more difficult to be achieved, and experience with low temperature salts has shown that the performance of the materials can degrade after moderate number of freeze–melt cycles. [13] This facts show that the research process is not completed so that these materials have not reached marketability yet.
Summing up, the advantages of this method are a high energy density even if the phase-change materials cannot save as much energy as the chemical reactions can. This aspect is discussed next.

2.2.3 Thermochemical reactions

The most efficient storage method is to convert the heat into chemical compounds, e.g. the Eva-Adams equation:

$$CH_4 + H_2O \leftrightarrow CO + 3H_2 \qquad [2],[41]$$

or the decomposition of methanol

$$CH_3OH \leftrightarrow CO + 2H_2 \qquad [2],[41]$$

have been proposed for the storage of solar energy. The chemical reactions involved must be completely reversible. With this method energy densities up to 250 kWh/m³ are possible, whereupon practically about 130 kWh/m³ can be achieved with pilot plants [24], which anyway represents the highest energy density of all presented energy storages; furthermore the energy can be saved over a large period of time at ambient temperature with only little losses. Unfortunately these systems are at an initial stage of research and far away from marketability, also the economics of this concept is still uncertain, but there is a potential that the performance can be improved and material and equipment cost can be reduced in mass production. In the future, these systems offer the prospect of power plants with inherent energy storage for continuous (24 h) generation of electricity. This issue will be increasingly significant as the world moves towards a truly renewable energy based economy. [13]

Further research is needed to improve understanding of the scientific and engineering characteristics of thermochemical TES systems and to help improve various aspects relating to the performance and implementation of these systems. The thermochemical material is a critical component of such systems. The cyclic behavior and degradation of thermochemical materials, as well as their cost, availability, durability and energy density are important parameters affecting the selection of a thermochemical material. Further research is needed on these topics, as well as on design factors, safety, size and efficiency, installation, maintenance and economics for thermochemical TES systems. [1]

2.3 Storage concept

There are two alternative high temperature storage concepts which are appropriate for different applications. They can be classified as active and passive systems, whereat the active systems can be subdivided into direct and indirect systems (Figure 2-4).

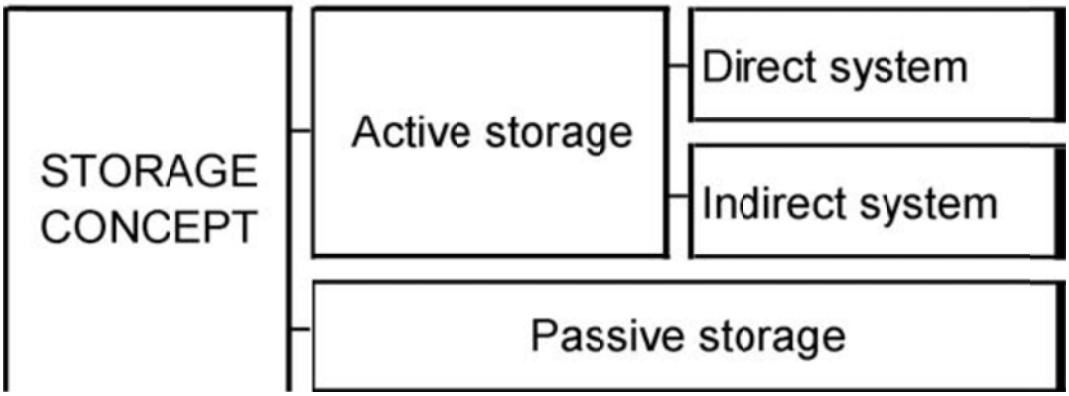

Figure 2-4: forms of storage concepts [8]

An active storage system is mainly characterized by forced convection heat transfer into the storage material. The storage medium itself circulates through a heat exchanger (this heat exchanger can also be either a solar receiver or a steam generator). In a direct system, the heat transfer fluid (HTF) serves also as the storage medium, while in an indirect system, a second medium is used for storing the heat. [13]

A passive storage system is classified by a dual medium storage system. The HTF passes through the collector and is piped to the storage where it increases the temperature of the storage material. When the energy is needed the HTF is pumped through the storage in reverse direction to heat the HTF (these systems are also called regenerators). During the charging and discharging it is directly in contact with the storage material or piped through a heat exchanger which is embedded in the storage tank. In this thesis, this kind of storage concept is investigated.

The main disadvantage of common regenerators is that the HTF temperature decreases during discharging, which leads to a decreasing efficiency of the heat engine. Another problem is the low heat transfer rate when a heat exchanger is used; packed beds reduce this problem, because the direct contact between HTF and storage material results in a higher heat transfer rate.

2.3.1 Active Systems

The main difference between direct and indirect active storage systems is that direct systems use the same fluid as HTF and storage material whereupon indirect systems use two different fluids. Both configurations can be built with one or two tanks whereupon two tank systems have the main advantage of higher fluid output temperatures because the cold and hot storage material can be stored separately. On the other hand, two tank solar systems have a lot of disadvantages which will not be rolled out at this point.
In active systems, molten salts are usually used as a HTF and storage material. These salts combine a high thermal capacity with a high boiling point, which makes it possible to store it unpressurised and eliminates the need for expensive heat exchangers.
The biggest problem of using molten salts as a HTF is their relatively high freezing point 120-220°C). The solidification in the pipes must be precluded because it could damage the power plant. To reduce this risk, routine freeze protection operations must be done by the thermal storage, which increases the maintenance and operating costs. [13] High costs of the material are also a disadvantage of these systems.
Active indirect systems avoid the freezing problematic by using different fluids as storage material and HTF but it is necessary to use an expensive heat exchanger to get the energy into the storage.

2.3.2 Passive Systems

Passive storage systems are characterized by a not circulating, mainly solid storage material which is charged and discharged by a circulating heat transfer fluid.
As storage material like rocks in a packed bed, concrete, bricks, PCMs or liquids which do not vaporize in the temperature range, can be utilized. When PCMs or liquids are used, a heat exchanger is necessary in order to transfer the thermal energy to the storage.
In this case the HTF can be every fluid, but usually oil is used because of its good performance in parabolic trough systems. Due to its unlimited availability the HTF hot air is applicative in solar tower power plants. These power plants profit from storages with a packed bed of stones because the storage can be charged and discharged without a heat exchanger even if the low thermal capacity results in a high mass flow rate.

The advantages of thermal storages containing solid material are the low cost of thermal storage media, high heat transfer rates into and out the solid medium, facility to handle of the material and in not air using systems the low degeneration of heat transfer between the heat exchanger and the storage material. [13]
On the other hand, these systems show only a few disadvantages. The main problems are the long-term instability of the storage material which can break into smaller parts as a result of the permanent thermal stress and as already mentioned the low thermal energy density. Not air based systems also have the disadvantage of a high cost heat exchanger which reduces the overall cost effectiveness.
Examples for these systems which were already realized are the “Midterm Storage Concepts –Further Development of Solid Storage Systems” [37] and a European project utilizing PCMs called DISTOR [38]. Both have been developed in cooperation with the German Aerospace Center.

2.4 Application area of thermal heat storages

Thermal heat storages can be used in several applications. As already mentioned in previous chapters, the integration of thermal storages in a power plant system is reasonable. But also in other applications thermal storages can help to economize fossil fuels or to increase the efficiency of existing processes.

2.4.1 Solar power plants

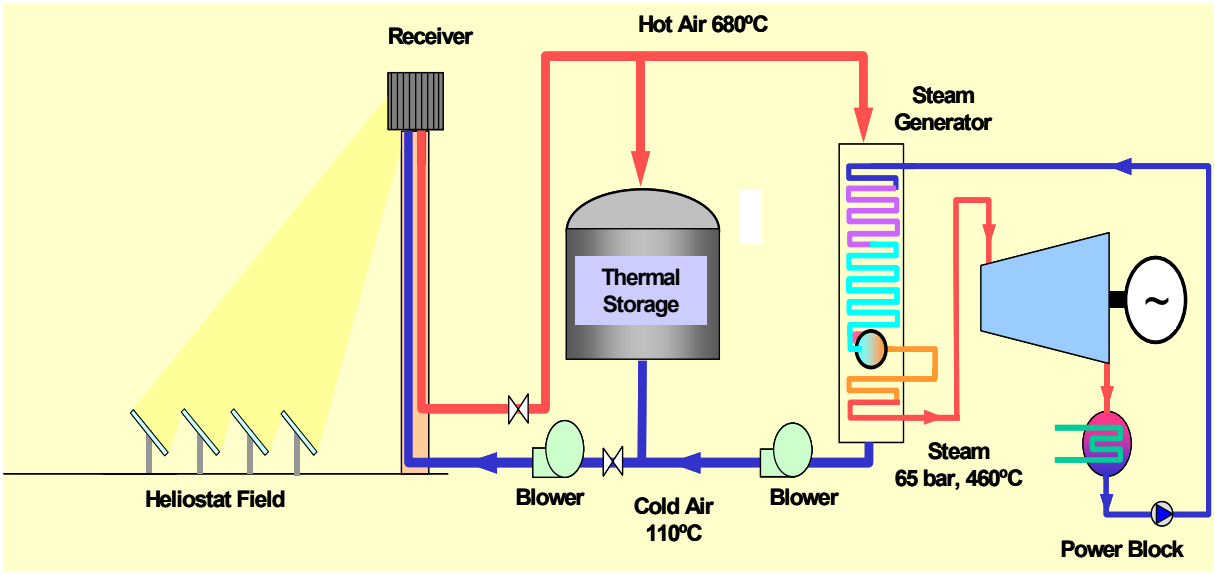

Figure 2-5: schematic of a solar tower power plant with hot air as heat transfer fluid

Figure 2-5 shows a sketch of a solar tower power plant utilizing hot air as heat transfer fluid. In opposition to the parabolic trough systems which use thermo oil as HTF, in many commercial solar power towers hot air is used to transport the heat to the steam generator. When this is the case, sensible heat storages containing packed beds are often used because they can utilize the hot air for loading directly. The advantage of this design is that additional attrition is avoided.
As already described in the introduction, heat storages have the potential to increase the effective use of thermal energy equipment and are necessary to produce solar generated power also in time of missing sunshine. So they are the basic component for correcting the mismatch between the supply and demand of energy [13]. In a future solar or semi-solar economy the heat storage of thermal power plants must be able to store the thermal energy for several hours of power generating to satisfy the high power demand in the evening hours.
Another reason for thermal energy storage is that it can be utilized as a buffer. If the solar radiation reduces over a short period of time, maybe because of a cloud covering the sun, the thermal storage can be discharged particularly to run the engines at constant and most efficient level. Power plants without storage in this case have to close the gap between supply of the solar field and demand of the engine with fossil fuels (hybrid plant) or reduce the engine performance.
Other designs using liquid sodium have been demonstrated, and systems using molten salts (40% potassium nitrate, 60% sodium nitrate) as the working fluids are now in operation. These working fluids have high heat capacities, which can be used to store the energy before using it to boil water to drive turbines. [18]

2.4.2 Other applications

The demand for flexible balancing power to maintain grid stability shows strong growth. This is where storage technology comes in: whenever supply exceeds demand, e.g. on a windy day, the power can be stored and then fed into the grid again during a calm. A promising approach is the adiabatic compressed-air energy storage. "Adiabatic" here means: additional use of the compression heat to increase efficiency.
Figure 2-6 shows the basic principle of this type of cavern pressure storage with the included thermal storage. When the air is compressed, the heat is not released into the surroundings: most of it is captured in a heat-storage facility. During discharge, the heat-storage device rereleases its energy into the compressed air, so that no gas co-combustion to heat the compressed air is needed. The object is to make

efficiencies of around 70% possible. Moreover the usage of a thermal storage can avoid the input of fossil fuels in this concept. Hence, this technology permits the CO_2-neutral provision of peak-load electricity from renewable energy. [32]

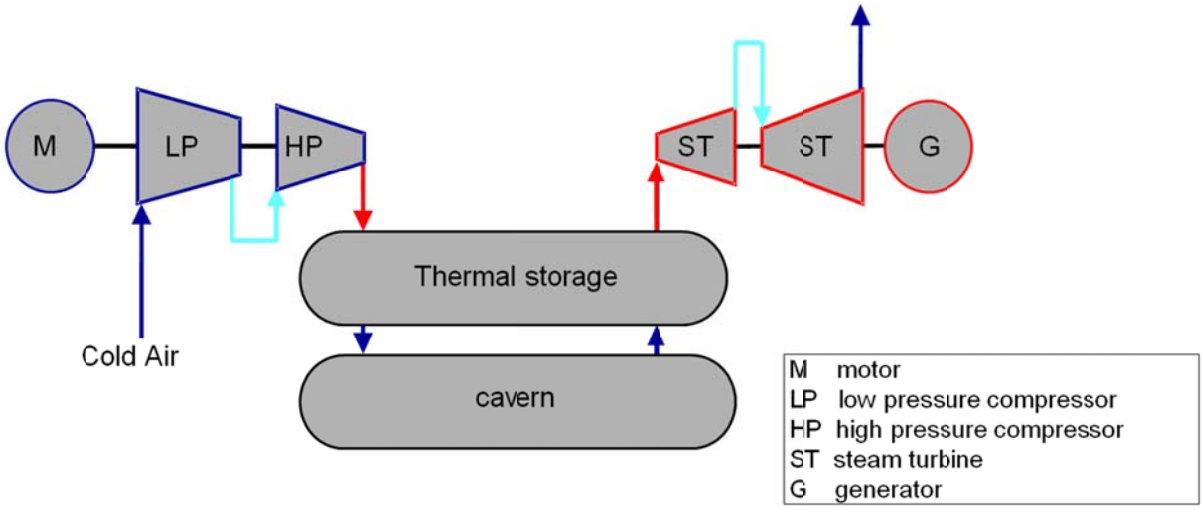

The only disadvantages of this technology are the high performance requirements of the compressors because gas with high temperatures has a larger volume.
Another point which should be considered is the profitability of such system, because the investment and capital cost of the plant must be amortized by the differences of the electricity rate during the day.

3 Fundamentals of numerical flow simulation

In this chapter the physical and mathematical background of CFD simulation is presented. Also the utilized simplifications of this kind of models are illustrated, so it can be explained how it is possible to compute such complex problem like turbulent flows in a short period of time.

3.1 Conservation laws

The physical fundamentals define conservation laws for mass, energy and momentum which cannot be violated. This knowledge leads to five conservation equations:

- mass conservation
- energy conservation
- momentum conservation x-direction
- momentum conservation y-direction
- momentum conservation z-direction

All modern CFD simulation tools use these five conservation equations to calculate the flow of gases and liquids. They can be written in integral and differential form and transformed to each other. The simulation program FLUENT and most of the other commercial software use the integral form and the Finite-Volume-Discretization which will be discussed in more detail later. For the calculation this method is better, because shocks which are discontinuities within the control volume are allowed.
On the other hand the differential form is more demonstrative, because it uses differentials. So in this thesis only this form is illustrated, but the derivation of the equations is not mentioned in this chapter, a more detailed look can be taken in scientific literature like “Stefan Lecheler 2011” [28].

3.1.1 Conservation of mass

The mass conservation equation is also called continuity equation. It describes the change of the mass over the time within a control volume, which is equal to the sum of all in- and outflows through the border of the control volume in x-, y- and z-direction resulting in the following equation after some modifications:

$$\frac{\partial}{\partial t}(\rho) + \frac{\partial}{\partial x}(\rho \cdot u) + \frac{\partial}{\partial y}(\rho \cdot v) + \frac{\partial}{\partial z}(\rho \cdot w) = 0 \qquad \text{eq. 3-1}$$

A more compact form of this equation is the divergence form. The velocities can be merged to the velocity vector $\vec{u}$.

$$\frac{\partial}{\partial t}(\rho) + \vec{\nabla} \cdot (\rho \cdot \vec{u}) = 0 \qquad \text{eq. 3-2}$$

3.1.2 Conservation of momentum

Analog to the conservation of mass, the conservation of momentum describes the change of momentum over time of a finite control volume. Momentum fluxes through the walls of the control volume are regarded as well as gravitational forces and friction. The friction can be subdivided into shear forces τ_{xy} and normal forces τ_{xx}. The following equations result after some transformation:

- x-momentum conservation equation in Cartesian coordinates:

$$\rho \cdot \left(\frac{\partial u}{\partial t} + u\frac{\partial u}{\partial x} + v\frac{\partial u}{\partial y} + w\frac{\partial u}{\partial z}\right) = g_x \cdot \rho - \frac{\partial p}{\partial x} + \frac{\partial}{\partial x}\overbrace{\left[2\mu\frac{\partial u}{\partial x} - \frac{2}{3}\mu\left(\frac{\partial u}{\partial x} + \frac{\partial v}{\partial y} + \frac{\partial w}{\partial z}\right)\right]}^{\tau_{xx}} + \frac{\partial}{\partial y}\overbrace{\left[\mu\left(\frac{\partial v}{\partial x} + \frac{\partial u}{\partial y}\right)\right]}^{\tau_{yx}} + \frac{\partial}{\partial z}\underbrace{\left[\mu\left(\frac{\partial u}{\partial z} + \frac{\partial w}{\partial x}\right)\right]}_{\tau_{zx}} \qquad \text{eq. 3-3}$$

- y-momentum conservation equation in Cartesian coordinates:

$$\rho \cdot \left(\frac{\partial v}{\partial t} + u\frac{\partial v}{\partial x} + v\frac{\partial v}{\partial y} + w\frac{\partial v}{\partial z}\right) = g_y \cdot \rho - \frac{\partial p}{\partial y} + \frac{\partial}{\partial x}\overbrace{\left[\mu\left(\frac{\partial u}{\partial y} + \frac{\partial v}{\partial x}\right)\right]}^{\tau_{xy}} + \frac{\partial}{\partial y}\overbrace{\left[2\mu\frac{\partial v}{\partial y} - \frac{2}{3}\mu\left(\frac{\partial u}{\partial x} + \frac{\partial v}{\partial y} + \frac{\partial w}{\partial z}\right)\right]}^{\tau_{yy}} + \frac{\partial}{\partial z}\underbrace{\left[\mu\left(\frac{\partial v}{\partial z} + \frac{\partial w}{\partial y}\right)\right]}_{\tau_{zy}} \qquad \text{eq. 3-4}$$

- z-momentum conservation equation in Cartesian coordinates:

$$\rho \cdot \left(\frac{\partial w}{\partial t} + u\frac{\partial w}{\partial x} + v\frac{\partial w}{\partial y} + w\frac{\partial w}{\partial z}\right) = g_z \cdot \rho - \frac{\partial p}{\partial z} + \frac{\partial}{\partial x}\overbrace{\left[\mu\left(\frac{\partial u}{\partial z} + \frac{\partial w}{\partial x}\right)\right]}^{\tau_{xz}} + \frac{\partial}{\partial z}\overbrace{\left[\mu\left(\frac{\partial v}{\partial z} + \frac{\partial w}{\partial y}\right)\right]}^{\tau_{yz}} + \frac{\partial}{\partial y}\underbrace{\left[2\mu\frac{\partial w}{\partial z} - \frac{2}{3}\mu\left(\frac{\partial u}{\partial x} + \frac{\partial v}{\partial y} + \frac{\partial w}{\partial z}\right)\right]}_{\tau_{zz}} \quad \textbf{eq. 3-5}$$

Where the first term represents the change of momentum over the time, the next two terms include the gravitation acceleration as well as moment fluxes through the borders of the control volume and the last three terms represent the shear and normal forces in the particular direction.

3.1.3 Energy conservation

The energy conservation is a well known physical principle and the conclusion of the first law of thermodynamics. In this equation a lot of forms of energy, like potential, kinetic and thermal energy, and their change over time have to be considered. Analog to the already presented conservation laws the following equation for the energy conservation is based on an infinite volume:.

$$\begin{aligned}\frac{\partial}{\partial t}\left[\rho \cdot \left(e + \frac{1}{2}\cdot\vec{u}^2\right)\right] &+ \frac{\partial}{\partial x}\left(\rho \cdot u\left(h + \frac{1}{2}\cdot\vec{u}^2\right) - \left(u\cdot\tau_{xx} + v\cdot\tau_{xy} + w\cdot\tau_{xz}\right) - \lambda\cdot\frac{\partial T}{\partial x}\right) \\ &+ \frac{\partial}{\partial y}\left(\rho \cdot v \cdot \left(h + \frac{1}{2}\cdot\vec{u}^2\right) - \left(u\cdot\tau_{yx} + v\cdot\tau_{yy} + w\cdot\tau_{yz}\right) - \lambda\cdot\frac{\partial T}{\partial y}\right) \\ &+ \frac{\partial}{\partial z}\left(\rho \cdot w \cdot \left(h + \frac{1}{2}\cdot\vec{u}^2\right) - \left(u\cdot\tau_{zx} + v\cdot\tau_{zy} + w\cdot\tau_{zz}\right) - \lambda\cdot\frac{\partial T}{\partial z}\right) \\ &- \rho\cdot\left(u\cdot g_x + v\cdot g_y + w\cdot g_z\right) - \rho\cdot\dot{q}_s = 0\end{aligned} \quad \textbf{eq. 3-6}$$

Where e is the total energy in the control volume and h is the specific enthalpy.

3.1.4 Navier–Stokes equations

In terms of physics the Navier-Stokes equations are only the momentum equation for flows. In the broader sense, especially in numerical fluid mechanics, this momentum equation is then expanded to a system of nonlinear partial differential equations of second order containing all conservation equations which were presented in the chapters before. In this case it is able to describe the fluid flow with all turbulences and eddies. Normally this equation system cannot be calculated analytically, only for some special cases, like a one dimensional flow over a planar plate, a non-numerical solution is possible. For more complex problems that is not feasible, so a numerical solution is necessary.
The Navier-Stokes equations combine the conservation equations to an equation system which can be described in different forms. Here only the more compact divergence form is presented. It is the most mathematical form and it is independent of a coordinate system.

$$\vec{u} = \begin{bmatrix} u \\ v \\ w \end{bmatrix} \quad \vec{g} = \begin{bmatrix} g_x \\ g_y \\ g_z \end{bmatrix} \quad \vec{\nabla} = \begin{bmatrix} \frac{\partial}{\partial x} \\ \frac{\partial}{\partial y} \\ \frac{\partial}{\partial z} \end{bmatrix} \quad I = \begin{bmatrix} 1 & 0 & 0 \\ 0 & 1 & 0 \\ 0 & 0 & 1 \end{bmatrix} \quad \tau = \begin{bmatrix} \tau_{xx} & \tau_{xy} & \tau_{xz} \\ \tau_{yx} & \tau_{yy} & \tau_{yz} \\ \tau_{zx} & \tau_{zy} & \tau_{zz} \end{bmatrix} \qquad \textbf{eq. 3-7}$$

$$\frac{\partial}{\partial t} \begin{bmatrix} \rho \\ \rho \cdot \vec{u} \\ \rho \cdot (e + \frac{1}{2} \cdot \vec{u}^2) \end{bmatrix} + \vec{\nabla} \begin{bmatrix} \rho \cdot \vec{u} \\ \rho \cdot \vec{u} \times \vec{u} + p \cdot I - \tau \\ \rho \cdot \vec{u} \cdot \left(h + \frac{1}{2} \cdot \vec{u}^2 \right) - \tau \cdot \vec{u} - \lambda \cdot \vec{\nabla} T \end{bmatrix} = \begin{bmatrix} 0 \\ \rho \cdot \vec{g} \\ \rho \cdot \vec{g} \cdot \vec{u} + \rho \cdot \dot{q}_s \end{bmatrix} \qquad \textbf{eq. 3-8}$$

where the velocity vector $\vec{u}$, the gravity vector $\vec{g}$, the divergence $\vec{\nabla}$, the identity matrix I and the stress matrix τ is used.

3.2 Discretization

As already mentioned, analytical solutions of these equations are only possible in a few special cases. So there is a need of methods which have the ability to solve the problems numerically. There are three methods to achieve this; every method has its special strengths and weaknesses and it depends on the case which one should be chosen. Therefore, these methods only should be broached in this paper, for a more detailed view Oertel and Böhle or Ferziger and Peric offer a comprehensive and detailed treatise for each method. [31], [10]

Finite difference method

The finite difference method is considered as the oldest method to solve partial differential equations. It consists of transforming the partial derivatives in difference equations over a small interval. It approximates the solutions to differential equations using finite difference equations to converge derivatives.

Finite element method

In the finite element method the differentials are described by shape functions such as parabolic equations. The variables are calculated within the simulation area by means of linear combination of the weighted shape function. The method is considered to be very flexible, but is less accurate than the finite-difference method.

Finite volume method

In the finite volume method, volume integrals in a partial differential equation that contain a divergence term are converted to surface integrals, using the divergence theorem. These terms are then evaluated as fluxes at the surfaces of each finite volume. Because the flux entering a given volume is identical to that leaving the adjacent volume, these methods are considered conservative. Another advantage of the finite volume method is that it is easily formulated to allow unstructured meshes. [8]

3.3 Mesh modeling

In order to generate a mesh for a flow region there are generally several possible element types, like hexahedron, prism, tetrahedral or pyramid element in 3D or triangular and quadratic elements in 2D. It is the user's choice which kind of mesh has more advantages in the special case.

3.3.1 Structured mesh

Structured meshes normally consist of hexahedrons in 3D or quadrates in 2D. This kind of mesh type can reduce the file size of a mesh because the addressing of each cell can be realized by a simple I,J,K coordinate system. For this reason it is also possible to reduce the computing time for a calculation, if a solver is used which is specially designed for structured meshes.

The downside of these meshes is that no automatic generation is possible hence it consumes a lot of time building such a mesh, which is an economical con. Therefore the usage of structured meshes on complex problems is unusual. [10]

3.3.2 Unstructured mesh

Unstructured meshes are more flexible than structured meshes. They can be generated automatically, which reduces the invested time of the user. In contrast to structured meshes they normally consist of tetrahedrons (3D) or triangles (2D), which increases the file size of the mesh. In 2D quadratic elements are also common or a mixture between these two types, in this special case the mesh is called hybrid mesh. Unfortunately the application of unstructured meshes leads to an increased demand for computing time. [10]

3.4 Turbulence modeling

This subchapter gives a brief overview of the alternative models which can apply for canal flow problems, the others will not be included. Also the mathematical background of the most common models will be explained. Generally one can say that the quality of simulation depends on the used model; every model has different requirements for the used grid and has to match the problem.
Almost all technical flows are turbulent. Turbulences are fluctuations with a high frequency at small scales. If the demonstrated Navier-Stokes equations in chapter 3.1, which are valid for all kinds of fluid flow simulations, were utilized, this would lead to a Direct Numerical Simulation (DNS) appreciating a transient calculation with small time steps. Moreover a very fine mesh would be needed to resolve the very small eddies. This solution of resolving turbulence flows would by far exceed the available computing power for any foreseeable future. [12] For this reason there are many turbulence models which are able to handle this problem with less computing power with only a small loss of precision, e.g. the Reynolds Averaged Navier-Stokes (RANS) Turbulence Models.

3.4.1 Introduction

The basic tool required for the derivation of the RANS equations from the instantaneous Navier–Stokes equations is the Reynolds decomposition. Reynolds decomposition refers to separation of the flow variable (like velocity u) into the mean (time-averaged) component ($\bar{u}$) and the fluctuating component (u'). Because the mean operator is a Reynolds operator, it has a set of properties. One of these properties is that the mean of the fluctuating quantity being equal to zero($\bar{u}' = 0$).

For the determination of the mean values two methods are used, the Reynolds Averaging for incompressible and the Favre-averaging for compressible flows.

Reynolds decomposition $$u(x,y,z,t) = \overline{u(x,y,z)} + u'(x,y,z,t)$$ **eq. 3-9**

Reynolds Averaging: $$\bar{f} = \frac{1}{T}\int_0^T f \cdot dt$$ **eq. 3-10**

Favre Averaging: $$\tilde{f} = \frac{\overline{\rho \cdot f}}{\bar{\rho}} \quad with \quad \overline{\rho \cdot f} = \frac{1}{T}\int_0^T (\rho \cdot f) \cdot dt$$ **eq. 3-11**

where T is the instant of time until the averaging takes place.
The pressure and the density are averaged by the eq. 3-10. All other variables are averaged by eq. 3-11:

$$\rho = \bar{\rho} + \rho' \qquad p = \bar{p} + p'$$
$$f = \tilde{f} + f'' \qquad \text{etc.}$$ **eq. 3-12**

Besides the already mentioned calculation rule there are some others which are relevant to introduce:

$$\frac{\overline{\partial f}}{\partial s} = \frac{\partial \bar{f}}{\partial s}\,;\, \overline{f+g} = \bar{f} + \bar{g}\,;\, \overline{\rho' \cdot \tilde{f}} = 0\,;\, \overline{\rho \cdot u''} = 0\,;\, \bar{\tilde{f}} = \tilde{f}$$ **eq. 3-13**

The following equation results from the conservation of mass and is transformed corresponding to eq. 3-12 and eq. 3-13.

$$\frac{\partial}{\partial t}(\bar{\rho}) + \frac{\partial}{\partial x}(\bar{\rho} \cdot \tilde{u}) + \frac{\partial}{\partial y}(\bar{\rho} \cdot \tilde{v}) + \frac{\partial}{\partial z}(\bar{\rho} \cdot \tilde{w}) = 0$$ **eq. 3-14**

The Reynolds averaged continuity equation (eq. 3-14) contains no fluctuating component. The only difference between this equation and eq. 3-1 is that averaged values are used.

3.4.2 Reynolds Averaged Navier-Stokes (RANS) equations

If the same transformation is done with the momentum conservation equations this leads to the Reynolds Averaged Navier-Stokes (RANS) equations which are introduced now for the three dimensions.

- x-direction:

$$\bar{\rho}\cdot\left(\frac{\partial\tilde{u}}{\partial t}+\tilde{u}\frac{\partial\tilde{u}}{\partial x}+\tilde{v}\frac{\partial\tilde{u}}{\partial y}+\tilde{w}\frac{\partial\tilde{u}}{\partial z}\right) = g_x\cdot\bar{\rho}-\frac{\partial\bar{p}}{\partial x}+\frac{\partial}{\partial x}\left[2\mu\frac{\partial\tilde{u}}{\partial x}-\frac{2}{3}\mu\left(\frac{\partial\tilde{u}}{\partial x}+\frac{\partial\tilde{v}}{\partial y}+\frac{\partial\tilde{w}}{\partial z}\right)\right] + \frac{\partial}{\partial y}\left[\mu\left(\frac{\partial\tilde{v}}{\partial x}+\frac{\partial\tilde{u}}{\partial y}\right)\right]+\frac{\partial}{\partial z}\left[\mu\left(\frac{\partial\tilde{u}}{\partial z}+\frac{\partial\tilde{w}}{\partial x}\right)\right] - \left(\frac{\partial\overline{(\rho\cdot u''^2)}}{\partial x}+\frac{\partial\overline{(\rho\cdot u''\cdot v'')}}{\partial y}+\frac{\partial\overline{(\rho\cdot u''\cdot w'')}}{\partial z}\right) \quad \text{eq. 3-15}$$

- y- direction:

$$\bar{\rho}\cdot\left(\frac{\partial\tilde{v}}{\partial t}+\tilde{u}\frac{\partial\tilde{v}}{\partial x}+\tilde{v}\frac{\partial\tilde{v}}{\partial y}+\tilde{w}\frac{\partial\tilde{v}}{\partial z}\right) = g_y\cdot\bar{\rho}-\frac{\partial\bar{p}}{\partial y}+\frac{\partial}{\partial x}\left[\mu\left(\frac{\partial\tilde{u}}{\partial y}+\frac{\partial\tilde{v}}{\partial x}\right)\right] + \frac{\partial}{\partial y}\left[2\mu\frac{\partial\tilde{v}}{\partial y}-\frac{2}{3}\mu\left(\frac{\partial\tilde{u}}{\partial x}+\frac{\partial\tilde{v}}{\partial y}+\frac{\partial\tilde{w}}{\partial z}\right)\right]+\frac{\partial}{\partial z}\left[\mu\left(\frac{\partial\tilde{v}}{\partial z}+\frac{\partial\tilde{w}}{\partial y}\right)\right] - \left(\frac{\partial\overline{(\rho\cdot v''\cdot u'')}}{\partial x}+\frac{\partial\overline{(\rho\cdot v''^2)}}{\partial y}+\frac{\partial\overline{(\rho\cdot v''\cdot w'')}}{\partial z}\right) \quad \text{eq. 3-16}$$

- z- direction:

$$\bar{\rho}\cdot\left(\frac{\partial\tilde{w}}{\partial t}+\tilde{u}\frac{\partial\tilde{w}}{\partial x}+\tilde{v}\frac{\partial\tilde{w}}{\partial y}+\tilde{w}\frac{\partial\tilde{w}}{\partial z}\right) = g_z\cdot\bar{\rho}-\frac{\partial\bar{p}}{\partial z}+\frac{\partial}{\partial x}\left[\mu\left(\frac{\partial\tilde{u}}{\partial z}+\frac{\partial\tilde{w}}{\partial x}\right)\right]+\frac{\partial}{\partial z}\left[\mu\left(\frac{\partial\tilde{v}}{\partial z}+\frac{\partial\tilde{w}}{\partial y}\right)\right] + \frac{\partial}{\partial y}\left[2\mu\frac{\partial\tilde{w}}{\partial z}-\frac{2}{3}\mu\left(\frac{\partial\tilde{u}}{\partial x}+\frac{\partial\tilde{v}}{\partial y}+\frac{\partial\tilde{w}}{\partial z}\right)\right]-\frac{\partial\overline{(\rho\cdot v''\cdot u'')}}{\partial x} + \frac{\partial\overline{(\rho\cdot v''^2)}}{\partial y}+\frac{\partial\overline{(\rho\cdot v''\cdot w'')}}{\partial z} \quad \text{eq. 3-17}$$

In contrast to the other conservation equations this transformation leads to a significant change of the momentum conservation equations. The last terms which appeared due to the transformation are called Reynolds stress and include the physics of the fluctuating components.
There is no closed system of equations. Put differently, there are more unknown than equations to solve them. This kind of problem is recognized as a closure problem. Therefore the variables for the Reynolds stress tensor have to be modeled with the turbulence models.

Reynolds stress tensor: $$\tau_T = \begin{pmatrix} \overline{-\rho \cdot u''^2} & \overline{-\rho \cdot u'' \cdot v''} & \overline{-\rho \cdot u'' \cdot w''} \\ \overline{-\rho \cdot v'' \cdot u''} & \overline{-\rho \cdot v''^2} & \overline{-\rho \cdot v'' \cdot w''} \\ \overline{-\rho \cdot w'' \cdot u''} & \overline{-\rho \cdot w'' \cdot v''} & \overline{-\rho \cdot w''^2} \end{pmatrix} \quad \text{eq. 3-18}$$

3.4.3 Reynolds Averaged Navier-Stokes (RANS) turbulence models

One class of turbulence models are the eddy viscosity models. These are turbulence models in which the Reynolds stresses, as obtained from a Reynolds averaging of the Navier-Stokes equations, are modeled by a linear constitutive relationship with the mean flow straining field. That is why they are also called Reynolds Averaged Navier-Stokes (RANS) Turbulence Models. They are the most economic approach for computing complex turbulent industrial flows. They are suitable for many engineering applications and typically provide the level of accuracy required. [12]
The basis of these models is known as the Boussinesq hypothesis [3]. In this approach the turbulent stress is treated analog to the viscous stress according to Stokes law:

$$\tau_{T\,i,j} = \mu_T \cdot \left(\frac{\partial \tilde{u}_i}{\partial x_j} + \frac{\partial \tilde{u}_j}{\partial x_i} \right) - \frac{2}{3} \delta_{i,j} \left(\bar{\rho} \cdot k + \mu_T \frac{\partial \tilde{u}_k}{\partial x_k} \right) \quad \text{eq. 3-19}$$

The Boussinesq hypothesis offers the option to calculate the Reynolds stress as a function of the mean velocity and eddy viscosity μ_T. This is not a material-dependent parameter like the kinematic viscosity μ but a place and time-dependent variable which is dependent to the geometrical dimensions and the average velocity. Consequently, the task of the following models is to return values for μ_T.
The models are named for the number of solving partial differential equations. If μ_T is only calculated algebraically the models are called zero-equation models. Moreover there are one- and two-equation models where only the most common models should

be presented in this thesis. For a more detailed view, Wilcox offers a good overview on this topic. [40]

3.4.3.1 k-ε Models

The standard k- ε model in ANSYS FLUENT has become the workhorse of practical engineering flow calculations in the time since it was proposed by Launder and Spalding. [27] Its robustness, economy, and reasonable accuracy for a wide range of turbulent flows explain its popularity in industrial flow and heat transfer simulations. The standard k- ε model is a two equation model that means it includes two extra transport equations to represent the turbulent properties of the flow. The first transported variable is turbulent kinetic energy, k. The second transported variable in this case is the turbulent dissipation, ε. It is the variable that determines the scale of the turbulence, whereas the first variable, k, determines the energy in the turbulence. For the turbulent viscosity, the following equation is valid:

$$\mu_T = C_\mu \cdot \rho \cdot \frac{k^2}{\varepsilon} \qquad \textbf{eq. 3-20}$$

The values for the turbulent kinetic energy k are calculated with the differential equation for their transportation. The sum of the temporal and convective change of k corresponds to the sum of diffusion, dissipation and production of k.

$$\rho \cdot \left(\frac{\partial k}{\partial t} + \tilde{u}\frac{\partial k}{\partial x} + \tilde{v}\frac{\partial k}{\partial y} + \tilde{w}\frac{\partial k}{\partial z}\right) = \frac{\partial\left[\left(\mu + \frac{\mu_T}{\sigma_k}\right)\frac{\partial k}{\partial x}\right]}{\partial x} + \frac{\partial\left[\left(\mu + \frac{\mu_T}{\sigma_k}\right)\frac{\partial k}{\partial y}\right]}{\partial y} + \frac{\partial\left[\left(\mu + \frac{\mu_T}{\sigma_k}\right)\frac{\partial k}{\partial z}\right]}{\partial z} - \rho \cdot \varepsilon + \tau_{T\,i,j} \cdot \frac{\partial u_i}{\partial x_j} \qquad \textbf{eq. 3-21}$$

Analog to the turbulent kinetic energy, their dissipation rate is calculated with the following equation:

$$\rho \cdot \left(\frac{\partial \varepsilon}{\partial t} + \tilde{u}\frac{\partial \varepsilon}{\partial x} + \tilde{v}\frac{\partial \varepsilon}{\partial y} + \tilde{w}\frac{\partial \varepsilon}{\partial z}\right) = \frac{\partial\left[\left(\mu + \frac{\mu_T}{\sigma_\varepsilon}\right)\frac{\partial \varepsilon}{\partial x}\right]}{\partial x} + \frac{\partial\left[\left(\mu + \frac{\mu_T}{\sigma_\varepsilon}\right)\frac{\partial \varepsilon}{\partial y}\right]}{\partial y} + \frac{\partial\left[\left(\mu + \frac{\mu_T}{\sigma_\varepsilon}\right)\frac{\partial \varepsilon}{\partial z}\right]}{\partial z} - C_{\varepsilon 2} \cdot \rho \cdot \frac{\varepsilon^2}{k} + C_{\varepsilon 1} \cdot \frac{\varepsilon}{k} \cdot \tau_{T\,i,j} \cdot \frac{\partial u_i}{\partial x_j} \quad \text{eq. 3-22}$$

Where the coefficients in the eq. 3-20 until eq. 3-22 are experimental values:

$$C_\mu = 0.09; \quad C_{\varepsilon 1} = 1.44; \quad C_{\varepsilon 2} = 1.92; \quad \sigma_k = 1.0; \quad \sigma_\varepsilon = 1.3$$

There are two major formulations of k-ε Models, realizable and standard and there are two important differences between the two types. First the realizable k-ε model contains an alternative formulation for the turbulent viscosity. Secondly a modified transport equation for the dissipation rate, ε, has been derived from an exact equation for the transport of the mean-square vorticity fluctuation.
On the contrary this very successful model has some drawbacks. It reacts very insensitively to adverse pressure gradients. Besides the standard k- ε model has problems with the boundary layer separation, which leads to resolution problems in the near wall region. [12]

3.4.3.2 k-ω Models

Another two equation model, which was supposed by Wilcox [40], is the k-ω model. Just as in the k-ε model, the first transported variable in this model is turbulent kinetic energy k. The second transported variable is the specific dissipation ω. The mathematical relationship between ε and ω can be expressed as

$$\omega = \frac{\varepsilon}{\beta^* \cdot k} \quad \text{eq. 3-23}$$

Moreover the equations for the turbulent viscosity and the turbulent kinetic energy also differ:

$$\mu_T = \rho \cdot \frac{k}{\omega} \quad \text{eq. 3-24}$$

$$\rho \cdot \left(\frac{\partial k}{\partial t} + \tilde{u}\frac{\partial k}{\partial x} + \tilde{v}\frac{\partial k}{\partial y} + \tilde{w}\frac{\partial k}{\partial z}\right) = \frac{\partial\left[\left(\mu + \frac{\mu_T}{\sigma_k}\right)\frac{\partial k}{\partial x}\right]}{\partial x} + \frac{\partial\left[\left(\mu + \frac{\mu_T}{\sigma_k}\right)\frac{\partial k}{\partial y}\right]}{\partial y} + \frac{\partial\left[\left(\mu + \frac{\mu_T}{\sigma_k}\right)\frac{\partial k}{\partial z}\right]}{\partial z} - \beta^* \cdot \rho \cdot k \cdot \omega + \tau_{T\,i,j} \cdot \frac{\partial u_i}{\partial x_j} \quad \text{eq. 3-25}$$

For the specific dissipation, a new equation is introduced. Similar to the turbulent dissipation it is calculated as the sum of the temporal and convective change of ω corresponding to the sum of diffusion, dissipation and production of ω.

$$\rho \cdot \left(\frac{\partial \omega}{\partial t} + \tilde{u}\frac{\partial \omega}{\partial x} + \tilde{v}\frac{\partial \omega}{\partial y} + \tilde{w}\frac{\partial \omega}{\partial z}\right) = \frac{\partial\left[\left(\mu + \frac{\mu_T}{\sigma_\omega}\right)\frac{\partial \omega}{\partial x}\right]}{\partial x} + \frac{\partial\left[\left(\mu + \frac{\mu_T}{\sigma_\omega}\right)\frac{\partial \omega}{\partial y}\right]}{\partial y} + \frac{\partial\left[\left(\mu + \frac{\mu_T}{\sigma_\omega}\right)\frac{\partial \omega}{\partial z}\right]}{\partial z} - \beta \cdot \rho \cdot \omega^2 + \alpha \cdot \frac{\omega}{k} \cdot \tau_{T\,i,j} \cdot \frac{\partial u_i}{\partial x_j} \quad \text{eq. 3-26}$$

According to Wilcox [40] the used coefficients have the following values:

$$\alpha = \frac{5}{9};\quad \beta = \frac{3}{40};\quad \beta^* = \frac{9}{100};\quad \sigma_\omega = 2;\quad \sigma_k = 2$$

The biggest advantage relative to the ε-equation is that the ω-equation can be integrated through the viscous sublayer without additional terms. Furthermore, k-ω models are typically better in predicting adverse pressure gradient boundary layer flows and separation. [12]
Nevertheless in a freestream flow the k- ω model produce not as good results as the k- ε model does.

3.4.3.3 Shear Stress Transport (SST)

The k-ω based Shear Stress Transport (SST) model combines the advantages of k-ω and k-ε models. Due to the included k-ω model, this model delivers better results in the viscous sublayer and in flows with a low Reynolds number. The problems of the k-ω model in the freestream and at the inflow region are solved in this model with the changeover to the k-ε model. This amalgamation is achieved by a transformation

of the k-ε model into a k-ω formulation. Furthermore some priority factors are introduced to the resulting equation to superpose the original k-ω equation. [14]
In this model the turbulent viscosity is calculated with the following equation:

$$\mu_T = \rho \cdot \frac{a_1 \cdot k}{\max(a_1 \cdot \omega, SF_2)} \qquad \text{eq. 3-27}$$

The equation for the turbulent kinetic energy is:

$$\rho \cdot \left(\frac{\partial k}{\partial t} + \tilde{u}\frac{\partial k}{\partial x} + \tilde{v}\frac{\partial k}{\partial y} + \tilde{w}\frac{\partial k}{\partial z}\right) = \frac{\partial\left[\left(\mu + \frac{\mu_T}{\sigma_{k3}}\right)\frac{\partial k}{\partial x}\right]}{\partial x} + \frac{\partial\left[\left(\mu + \frac{\mu_T}{\sigma_{k3}}\right)\frac{\partial k}{\partial y}\right]}{\partial y} + \frac{\partial\left[\left(\mu + \frac{\mu_T}{\sigma_{k3}}\right)\frac{\partial k}{\partial z}\right]}{\partial z} - \beta' \cdot \rho \cdot k \cdot \omega + \tau_{T\,i,j} \cdot \frac{\partial u_i}{\partial x_j} \qquad \text{eq. 3-28}$$

And the equation for the specific dissipation rate is:

$$\rho \cdot \left(\frac{\partial \omega}{\partial t} + \tilde{u}\frac{\partial \omega}{\partial x} + \tilde{v}\frac{\partial \omega}{\partial y} + \tilde{w}\frac{\partial \omega}{\partial z}\right) = \frac{\partial\left[\left(\mu + \frac{\mu_T}{\sigma_{\omega 3}}\right)\frac{\partial \omega}{\partial x}\right]}{\partial x} + \frac{\partial\left[\left(\mu + \frac{\mu_T}{\sigma_{\omega 3}}\right)\frac{\partial \omega}{\partial y}\right]}{\partial y} + \frac{\partial\left[\left(\mu + \frac{\mu_T}{\sigma_{\omega 3}}\right)\frac{\partial \omega}{\partial z}\right]}{\partial z} - \beta_3 \cdot \rho \cdot \omega^2 + \alpha_3 \cdot \frac{\omega}{k} \cdot \tau_{T\,i,j} \cdot \frac{\partial u_i}{\partial x_j} + (1 - F_1)\frac{2 \cdot \rho}{\sigma_{\omega 2} \cdot \omega} \cdot \left(\frac{\partial k}{\partial x} + \frac{\partial k}{\partial y} + \frac{\partial k}{\partial z}\right) \cdot \left(\frac{\partial \omega}{\partial x} + \frac{\partial \omega}{\partial y} + \frac{\partial \omega}{\partial z}\right) \qquad \text{eq. 3-29}$$

For the parameters used in eq. 3-27, eq. 3-28 and eq. 3-29, the following definitions are valid:

$$F_1 = \tanh(arg_1{}^4) \;\; with \;\; arg_1 = min\left[max\left(\frac{\sqrt{k}}{\beta' \cdot \omega \cdot y}, \frac{500\nu}{y^2 \cdot \omega}\right), \frac{4\rho k}{CD_{kw} \cdot \sigma_{\omega 2} y^2}\right] \qquad \text{eq. 3-30}$$

$$CD_{kw} = max\left[\frac{2\rho}{\sigma_{\omega 2} \cdot \omega}\left(\frac{\partial k}{\partial x} + \frac{\partial k}{\partial y} + \frac{\partial k}{\partial z}\right) \cdot \left(\frac{\partial \omega}{\partial x} + \frac{\partial \omega}{\partial y} + \frac{\partial \omega}{\partial z}\right), 10^{-10}\right] \qquad \text{eq. 3-31}$$

$$F_2 = \tanh(arg_2^2) \quad with \quad arg_2 = \max\left(\frac{2\sqrt{k}}{\beta' \cdot \omega \cdot y}, \frac{500\nu}{y^2 \cdot \omega}\right) \qquad \text{eq. 3-32}$$

$$S = \frac{1}{2}\left(\frac{\partial \tilde{u}_i}{\partial x_j} + \frac{\partial \tilde{u}_j}{\partial x_i}\right) \qquad \text{eq. 3-33}$$

$$\beta' = 9/100 \qquad a_1 = 0.31$$

$$y = distance\ to\ the\ nearest\ wall$$

Averaging provision for the following variables $\Phi_3 = F_1 \Phi_1 + (1 - F_1)\Phi_2$

$$\alpha_1 = 5/9 \qquad \alpha_2 = 0.44$$

$$\beta_1 = 3/40 \qquad \beta_2 = 0.0828$$

$$\sigma_{k1} = 2 \qquad \sigma_{k2} = 1$$

$$\sigma_{\omega 1} = 2 \qquad \sigma_{\omega 2} = 1/0.856$$

There is a term which appears in all terms of the production rate, here it is written completely:

$$\tau_{T\,i,j} \cdot \frac{\partial u_i}{\partial x_j} = \begin{bmatrix} \left(\frac{\partial \tilde{u}}{\partial x} + \frac{\partial \tilde{u}}{\partial x}\right) \cdot \frac{\partial \tilde{u}}{\partial x} + \left(\frac{\partial \tilde{u}}{\partial y} + \frac{\partial \tilde{v}}{\partial x}\right) \cdot \frac{\partial \tilde{u}}{\partial y} + \left(\frac{\partial \tilde{u}}{\partial z} + \frac{\partial \tilde{w}}{\partial x}\right) \cdot \frac{\partial \tilde{u}}{\partial z} \\ + \left(\frac{\partial \tilde{v}}{\partial x} + \frac{\partial \tilde{u}}{\partial y}\right) \cdot \frac{\partial \tilde{v}}{\partial x} + \left(\frac{\partial \tilde{v}}{\partial y} + \frac{\partial \tilde{v}}{\partial y}\right) \cdot \frac{\partial \tilde{v}}{\partial y} + \left(\frac{\partial \tilde{v}}{\partial z} + \frac{\partial \tilde{w}}{\partial y}\right) \cdot \frac{\partial \tilde{v}}{\partial z} \\ + \left(\frac{\partial \tilde{w}}{\partial x} + \frac{\partial \tilde{u}}{\partial z}\right) \cdot \frac{\partial \tilde{w}}{\partial x} + \left(\frac{\partial \tilde{w}}{\partial y} + \frac{\partial \tilde{v}}{\partial z}\right) \cdot \frac{\partial \tilde{w}}{\partial y} + \left(\frac{\partial \tilde{w}}{\partial z} + \frac{\partial \tilde{w}}{\partial z}\right) \cdot \frac{\partial \tilde{w}}{\partial z} \end{bmatrix} \cdot \mu_T$$
$$- \frac{2}{3}\left[\bar{\rho} \cdot k + \mu_T\left(\frac{\partial \tilde{u}}{\partial x} + \frac{\partial \tilde{v}}{\partial y} + \frac{\partial \tilde{w}}{\partial z}\right)\right] \cdot \left(\frac{\partial \tilde{u}}{\partial x} + \frac{\partial \tilde{v}}{\partial y} + \frac{\partial \tilde{w}}{\partial z}\right) \qquad \text{eq. 3-34}$$

3.4.4 Wall treatment

The wall treatment is an important part of adapting the individual mesh to the used turbulence model because the different models have different requirements in the near-wall region. It is obvious that a model like the k- ε model which has problems with the resolution in the near-wall regions needs another wall treatment as the k-ω model.

But there are basic physical phenomena which are valid for every kind of turbulence flows for example that turbulent flows are significantly affected by the presence of walls. [11], [5] Also the no-slip condition at the wall has to be satisfied which means that very close to the wall, viscous damping reduces the tangential velocity fluctuations, while kinematic blocking reduces the normal fluctuations. [11]

In general you can say that the near-wall treatment affects the fidelity of numerical simulations, because walls are the main source of turbulence. [11], [5]
So the main challenge for the creation of a good mesh is the design in the near-wall regions. For the simulation of the flow near walls there are two approaches to handle with the boundary layer. In one approach the layers which are nearest to the wall are not resolved. Instead semi-empirical formulas called wall-functions are used to bridge the viscosity-affected region between the wall and the fully-turbulent region. [11], [5]
In the other approach the near-wall region is resolved all the way to the wall. The cells in this approach have to scale down until the minimum cell size, also called spacing, is reached. Here the turbulence models ought to be valid throughout the near-wall region

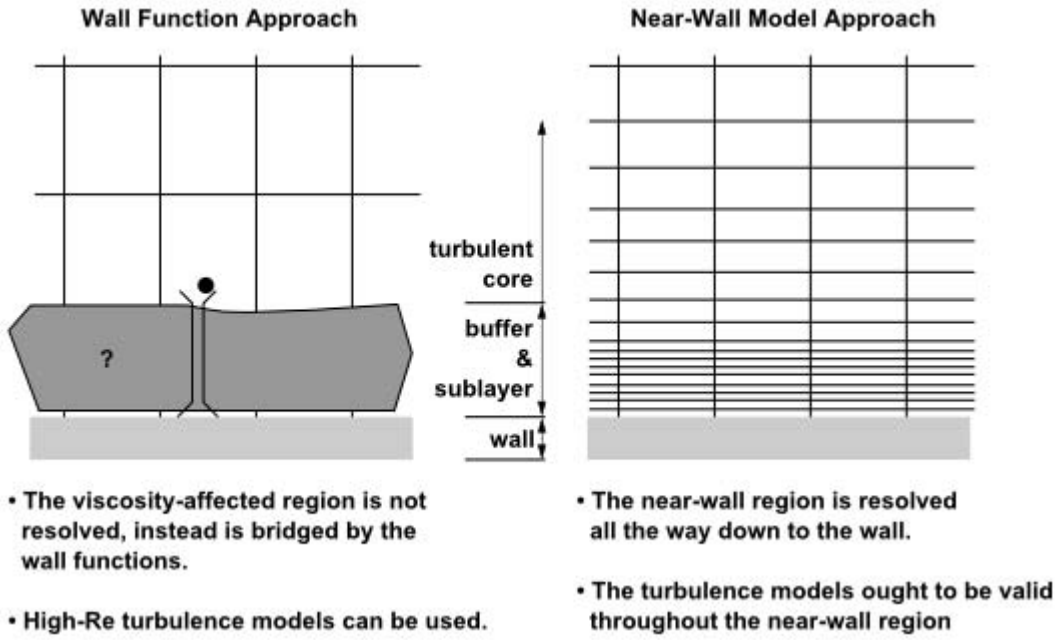

Figure 3-1 : different approaches for the near-wall region [11]

Figure 3-1 outlines the presented facts in a compact form and recapitulates the most important points.
In order to evaluate the suitability of a mesh and a wall treatment a value called y^+ is introduced. It can be defined in the following way:

$$y^+ = \frac{u_* \cdot y}{\nu} \quad with \quad u_* = \sqrt{\frac{\tau_w}{\rho}} \qquad \text{eq. 3-35}$$

In this equation u_* is the friction velocity at the nearest wall, y is the distance to the nearest wall and v is the local kinematic viscosity of the fluid. The friction velocity is dependent on wall shear stress which can be calculated with the following equation:

$$\tau_W = \rho \cdot \nu \cdot \frac{\partial y}{\partial x}\Big|_{y=0} \qquad \text{eq. 3-36}$$

The ideal value margin for y^+ depends on the turbulence model and on the usage of a wall function. For example SST and k-ω models require $y^+ \leq 1$ [11] on the other side for k- ε models with classical wall function a value of $30 < y^+ < 300$ [33] are desirable. The reason is that the grid in k- ε models near the wall must not be so fine that the computation point lies outside the logarithmic law of the wall. [19]

3.5 Porous media model

Many industrial applications involve the modeling of flow through porous media, such as filters, catalyst beds, and packing. A simulation of storage material needs a special handling. In case of honeycomb or hexagonal bricks it would be imaginable to model a complex geometry with thousands of little pipes in it. In the case of packed beds even such numerically extensive solution is not thinkable.
In order to resolve this problem, various porous media models were invented which convert the porous region into an additional equation which can be solved numerically like the already presented equations. Of course in these equations there are parameters which have to be adapted in the special case, e.g. the porosity or the particle diameter.
In the following pages some general porous media models are presented and then a more detailed look at the model used in FLUENT will be given.

3.5.1 Introduction

K.A.R. Ismail and R. Stuginsky Jr. [22] presented six different models for the porous media in fixed beds which vary hard in complexity. A great deal of published work on fixed bed energy storage uses the model originally developed by Schumann. This model is a two phase transient and one dimensional which enables prediction of the axial and temporal distribution of the solid and fluid temperatures. Other models are simpler, which leads to a reduced computation time. Their capability to predict exact results, depends on the simplification of the model and if this simplification is suitable in the special case. The introduced models differ in the quantity of phases (one and

two phase models), the character of the solver (transient or steady) and the number of dimensions (one and two dimensions). [22]
If the thermal conductivity and thermal capacity of the storage material compared to the working fluid is very high and the heat transfer area is very large, it is possible to stop differencing between the solid's and the fluid's location-dependent temperature. This kind of model is named one phase or homogeneous model. If such simplification is impossible a two phase or heterogeneous model is used. Here the temperatures of the fluid and solid are calculated separately.

3.5.2 Porous media model in FLUENT

The used porous media model in ANSYS FLUENT is a one phase model, which referring to chapter 3.5.1 means that there is no differentiation between the local temperature in the fluid and solid.
The calculation in the porous area can be accomplished with the physical or the superficial velocity. The correlation of these two velocities can be calculated with the following equation:

$$v_{\infty} = \varepsilon \cdot v_{physical} \qquad \text{eq. 3-37}$$

Corresponding to the FLUENT User Guide [12] calculations with the true (physical) velocity are more accurate, so for the following equations v = $v_{physical}$ is valid. Therefore the energy conservation equation in the porous model can be described with the following equation. The subscript f tags the variables of the fluid whereas the subscript s the parameters of the solid.

$$\frac{\partial}{\partial t}\left(\varepsilon \cdot \rho_f \cdot E_f + (1-\varepsilon) \cdot \rho_s \cdot E_s\right) + \nabla \cdot \left(\varepsilon \cdot \vec{v}\left(\varepsilon \cdot \rho_f \cdot E_f + p - \vec{\vec{\tau}}\right)\right) = \nabla \cdot \left(\lambda_{eff} \cdot \nabla T\right) + S_f^h \quad \text{with } \lambda_{eff} = \varepsilon \cdot \lambda_f + (1-\varepsilon) \cdot \lambda_s \qquad \text{eq. 3-38}$$

where E_f is the total fluid energy, E_s is the total solid medium energy, λ_{eff} is the effective thermal conductivity of the medium and S_f^h the fluid enthalpy source term. The effective thermal conductivity consists of the fluid phase thermal conductivity λ_f (including the turbulent contribution, λ_t) and the solid medium thermal conductivity λ_s. This equation contains the terms of the energy conservation equation (eq. 3-6) for the fluid and the solid with modifications to the conduction flux and the transient terms only. In the porous medium, the conduction flux uses an effective conductivity

and the transient term includes the thermal inertia of the solid region on the medium. [12]

Porous media are modeled by the addition of a momentum source term to the standard fluid flow equations. This term is affected by the pressure loss during the transition of the porous media zone which is proportional to the fluid velocity (or velocity squared) in the cell. [12] It is taken into account by the source term of the momentum conservation equation. Since the solid is immovable, only the fluid between the solid particles is taken into account in the following equation. This media contains the shear stress .

$$\frac{\partial(\varepsilon \cdot \rho \cdot \vec{v})}{\partial t} + \vec{\nabla} \cdot \left(\varepsilon \left(\rho \cdot \vec{v} \cdot (\vec{v})^T + p - \vec{\vec{\tau}}\right)\right) = -\mu \cdot \vec{\alpha}_* \times \vec{v} + 0.5 \cdot \rho \cdot |\vec{v}| \cdot \vec{C}_2 \times \vec{v}$$

$$\text{with} \quad \vec{\alpha}_* = \begin{pmatrix} \frac{1}{\alpha_x} \\ \frac{1}{\alpha_y} \\ \frac{1}{\alpha_z} \end{pmatrix} \qquad \textbf{eq. 3-39}$$

The used variables in this equation are properties of the fluid or solid, excepting $\vec{C}_2$ which is the inertial resistance factor and $\vec{\alpha}_*$ which is the permeability. They are input values for the creation of a porous media zone and have to be calculated referring to the superficial velocity.

4 Simulation of thermal storages

In this chapter it will be given an overview to the examined geometry and the motivation for the used models for the simulation will be explained. It will also straighten out the basic problem of the flow distribution in thermal storages and describe the approach to solve the task.

4.1 Geometry of the examined heat storage

Figure 4-1 illustrates an exemplary geometry of a storage tank. The storage geometry consists of a cylinder wherein the storage material resides (in cyan). On both ends of the cylinder a funnel shaped flow distributor makes the connection to the inlet and outlet pipe. The function of this diffuser is to distribute the stream of hot air, but it also converts the kinetic energy of the fluid into potential energy or vice versa by slowing down the fluid's velocity. This leads to an increased pressure at the beginning of the packed bed.

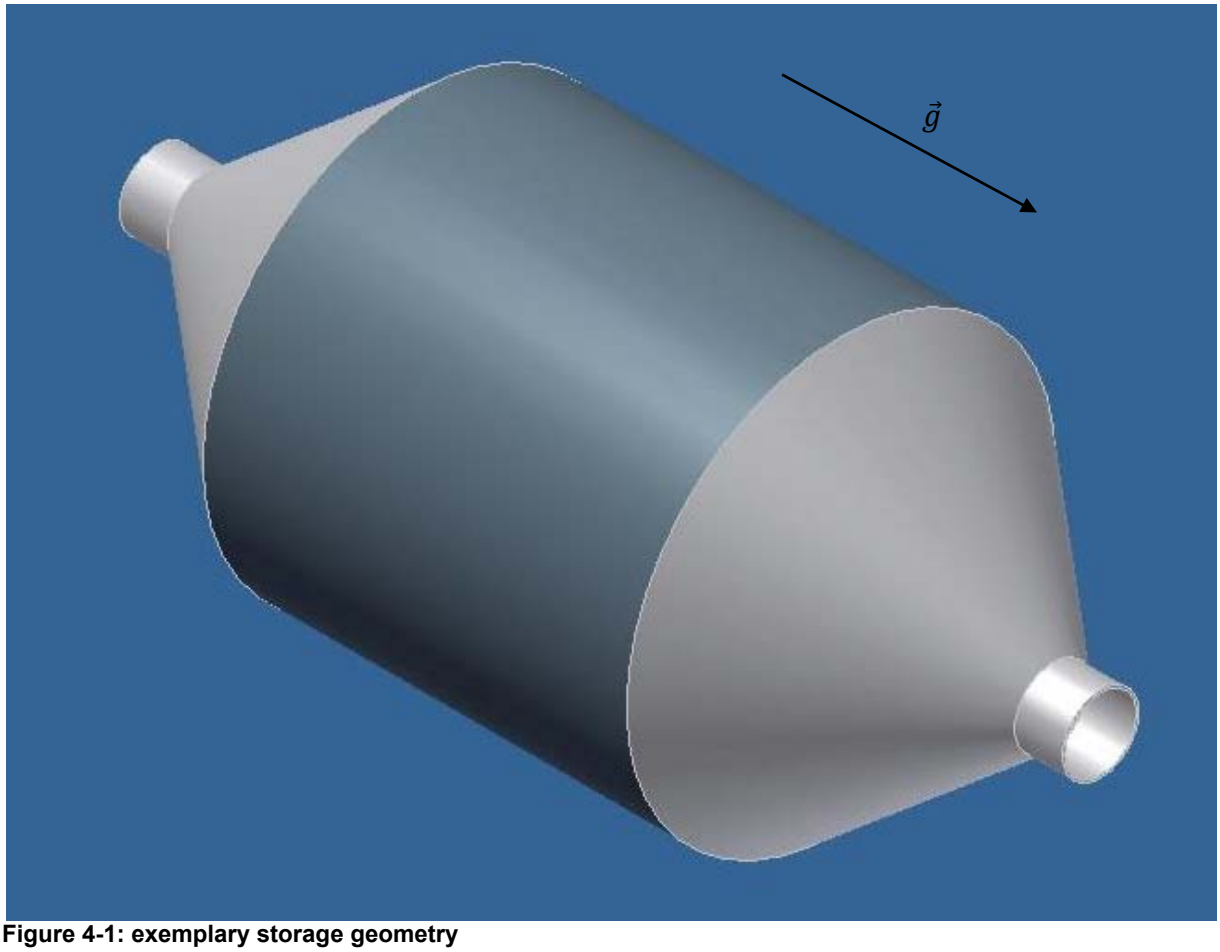

Figure 4-1: exemplary storage geometry

The geometry is rotational symmetric; expressed in cylindrical coordinates the solid figure can be described with the three coordinates x, r and φ. The flow parameters change in the direction of x and r and are independent of the angle φ. Moreover the two dimensional figure is axially symmetric. In reality the storage tank is coated by a thick insulation which is not pictured in this illustration. For the use in a power station the tank is normally positioned in a vertical direction so only one perforated plate for the fixation of the bed material is needed. In the picture it is displayed in another way for the sake of clarity. Also for the simulation the geometry of the storage is placed horizontally, which is no problem as the gravity vector shows in the correct direction.

4.1.1 Parameters of a heat storage

The basic geometry parameters which influence the flow characteristics are the height of the diffuser h_v, the diameter of the inlet tube d_{in}, the diameter D and the height H of the storage tank and are summarized in Figure 4-2.

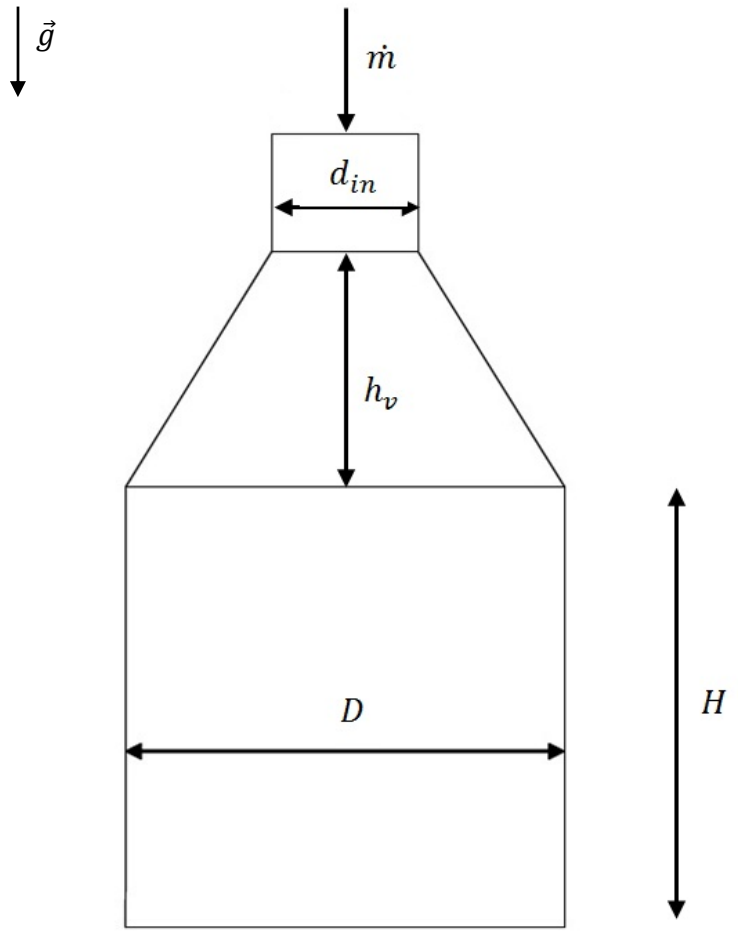

Figure 4-2: sketch inlet area

Furthermore there are two parameters that describe the fluid flow and influence the distribution as well: The mass flow rate $\dot{m}$ and the temperature of the fluid T_{in} that defines the density and the viscosity of the inflowing air. The velocity at the inlet is a derivate of the mass flow and the inlet diameter and represents also an important value because it constitutes the upper limit of the mass flow rate. eq. 4-1 shows that the fluid's velocity affects the pressure drop. Therefore higher velocities would lead to worse energy balance of the whole storage system.

4.1.2 Dimensionless parameters

Since the task is to compare different storage geometries, the large number of parameters must be reduced for an effective comparison. There are two possibilities to achieve this. The first possibility is to reduce the system of parameters to the most important. The other possibility is to merge the existing parameters into parameters of a higher order.
Due to this approach it is necessary to find parameters which enable a statement on the flow conditions and make the diffuser geometry comparable. These parameters can be found in earlier papers on this topic [34] [29] or concerning fluid flow through packed beds [2]. It is also part of this thesis to validate the correctness of the used parameters.
In addition it is relevant to mention that there is an important parameter which is able to quantify the effects of the pressure drop on the flow distribution in a packed bed.

pressure drop
The flow distribution is directly affected by the pressure drop; a high pressure drop leads to a better flow distribution. This becomes apparent if one imagine the pressure drop as a potential difference between inlet and outlet. So the fluid is pressed through the porous barrier utilizing every free space between the particles, resulting in a better flow distribution.
But a high pressure drop also has a negative impact on the energy balance of the storage system because this leads to a higher power demand of the pumps and fans.
The pressure drop per length can be calculated with equation eq. 4-1:

$$\frac{|\Delta p|}{H} = \frac{150 \cdot \mu \cdot (1-\varepsilon)^2}{D_p^2 \cdot \varepsilon^3} \cdot v_\infty + \frac{1.75 \cdot \rho \cdot (1-\varepsilon)}{D_p \cdot \varepsilon^3} \cdot v_\infty^2 \qquad \text{eq. 4-1}$$

It can be seen that the pressure drop hardly depends on the porosity of the used storage material, the fluid's superficial velocity v_∞ and the particle diameter D_p.

ε represents a fraction of the volume of voids over the total volume and according to that $0 \leq \varepsilon \leq 1$ is true. The formula also includes the density of the fluid ρ and the dynamic viscosity μ. The pressure drop is also affected by the height of the storage bed H. It is the only existing influence of the storage's height on the flow distribution.
One can say that equation eq. 4-1 returns good values because the calculated values for the pressure drop correspond almost exactly with the values extracted of the simulations.

Euler number

In order to receive comparable results for different geometries of heat storages another characteristic is necessary. The so called Euler number expresses the relationship between the local pressure drop Δp in the porous media of the storage and the kinetic energy per volume of the streaming fluid. It is used to characterize losses in the flow, where a perfect frictionless flow corresponds to an Euler number of 1. The relative kinetic energy can be calculated with the density of the fluid ρ and the physical velocity in the porous media of the fluid v.

$$Eu = \frac{\Delta p}{\rho \cdot v^2} \qquad \text{eq. 4-2}$$

In a recent study, Lier 2008 [29] performed simulations for pressurized sensible heat storages containing packed beds and found that the values for the Euler number should be larger than 400 to achieve a good flow distribution for any storage geometry with a truncated cone flow distributor. This result could not be validated in this study, instead Euler numbers of 600 are considered as the minimum.

Reynolds number

Another important and well known dimensionless parameter is the Reynolds number that gives a measure of the ratio of inertial forces to viscous forces and consequently quantifies the relative importance of these two types of forces for given flow conditions. It can be calculated with the inlet velocity v, the inlet diameter d_{in} and the kinematic viscosity ν which is affected by the inlet temperature of the fluid.

$$Re = \frac{v_{in} \cdot d_{in}}{\nu(T_{in})} = \frac{4 \cdot \dot{m}}{\rho(T_{in}) \cdot \nu(T_{in}) \cdot \pi \cdot d_{in}} \qquad \text{eq. 4-3}$$

The Reynolds number unite both flow parameters, $\dot{m}$ and T_{in} to one dimensionless parameter.

Ψ-Parameter

The third dimensionless parameter that should be introduced is Ψ. This parameter is used for the comparison of different frustoconical diffuser geometries and has been adapted for the use of thermal storages with packed beds. In contrast to the Reynolds number which is a function of the fluid flow parameters Ψ only depends on the already introduced geometry parameters of the storage.

$$\Psi = \Psi_1 \cdot \Psi_2 = \frac{D^3}{h_v \cdot d_{in}^2} \quad \text{with} \quad \Psi_1 = \frac{D}{h_v}, \Psi_2 = \left(\frac{D}{d_{in}}\right)^2 \qquad \textbf{eq. 4-4}$$

These dimensionless parameters include all parameters which were introduced in chapter 4.1.1. The Euler number includes the height H and determines the lower limit for this parameter. The Ψ-Parameter merges all geometry parameter as the Reynolds number all flow parameter. Therefore,

Lier 2008 [29] made the assumption that these two variables (Re and Ψ) suffice to compare the flow distribution of two different geometries of thermal storages. The verification of this hypothesis is also part of this research and will be examined in the chapter 5.2.1.

4.2 Modeling a basic storage geometry

This chapter has been divided into four sections. First a justification will be given not only for the simplifications and cutbacks of the model but also for the boundary conditions which reduce the complexity as well. Section three goes on to explain the used techniques and calculation methods which were adapted in the simulation. Finally the meshing process but not the mesh independence study will be introduced.

4.2.1 Geometry simplification

Due to the rotational symmetry of the heat storage and the independence of the flow parameters of the third dimension, the angle φ, the geometry can be calculated in two dimensions. This economizes a lot of calculation time and reduces the complexity of meshing. The complexity of the problem can be reduced another time by cutting the cross section in the middle. As the investigation zone is located at the entry of the porous zone only the front half of the storage is simulated. It could be validated that this simplification has no effect on the flow distribution in the reviewed region.

4.2.2 Model boundary conditions

There are few basic boundary conditions and simulation preconditions which are considered as constant values for all accomplished simulations.
Above all it is relevant to mention that the storage is assumed as adiabatic. Since in the real case there would be spent a lot of effort to insulate the storage, it is justifiable to make this supposition.
Obviously, every storage geometry needs an inlet and an outlet; both are defined as boundary conditions for the storage which have to be defined with three parameters. Two of them are variable: The hydraulic diameter which is equal to the inlet diameter and the mass flow rate at this system border. The last parameter here is the turbulent intensity, it is assumed to be 10%. In case of a reduced geometry the outlet is located in the middle of the porous zone, so the turbulent intensity can be set equal to zero and the hydraulic diameter is on a par with the diameter of the storage.
The last values that are constant over all simulations are the parameters for the porous media zone. The porosity of the storage material and the particle diameter are experimental values for a packed bed of basalt stones. The particle diameter can be calculated with eq. 4-1 with given preconditions for a example geometry. Therefore, in all simulations $\varepsilon = 0.37$ and $D_p = 0.063m$ can be considered as true.

4.2.3 Selection of the turbulence model and solution methods

At this point it is important to adopt the theoretical knowledge presented in chapter 2 onto the simulation model. Due to large diameters and easy geometry, without acute angles that affect the boundary layer, the standard k-ε model with standard wall function seems to be a good choice. It should deliver good results with the usage of little computational resources. Moreover the SST model would be possible and in tests it delivers as good results as the k-ε model but with a longer computation time. The k-ω model is not helpful at this point because a closer inspection of the near wall region is not necessary. As a result of the usage of the standard wall function, a value for $y^+ > 30$ is necessary.
After the decision for a turbulence model the solver has to be chosen and initialized. The decision was made in favor of a pressure based solver. Subsequently the spatial discretization for pressure, momentum, turbulent kinetic energy, turbulent dissipation rate and energy have to be selected.
Following the FLUENT User Guide [12], the PRESTO! scheme is suitable for flows with high swirl numbers, high-Rayleigh-number natural convection, high-speed rotating flows, flows involving porous media, and flows in strongly curved domains,

thus this scheme should be chosen. For the other equations the decision must be made between the first and second order upwind scheme. While the first-order discretization generally yields better convergence than the second-order scheme, it generally will yield less accurate results. [12] For any kind of meshes, the usage of the second-order discretization will obtain better results. On the other hand this method needs more computation time but as it delivers more exact results for the flow distribution it thus justifies the effort.
Finally the simulation is initialized hybrid. This solution method is a collection of recipes and boundary interpolation methods. It solves the Laplace equation to produce a velocity field that conforms to complex domain geometries, and a pressure field which smoothly connects high and low pressure values in the computational domain. All other variables (i.e. temperature, turbulence, VOF, species, etc.) will be patched based on domain averaged values or a predetermined recipe. [11]

4.2.4 Meshing the storage geometry

The meshing of the geometry is a very critical step in the process of simulation. For this study it was created with the mesh-generator ICEM.
The quality of the mesh has a great influence on the grade of the whole simulation. Consequently it consumes a lot of time to generate an adequate mesh and to verify its independence.
It is also important that the mesh structure fits to the problem. Structured meshes are not practicable for the reviewed problem because an automated generation is not possible with this mesh type. For this reason unstructured meshes are selected for the meshing of the storage, here the mesh generation process can be automated. This criterion is essential for the generation of a large number of geometries.
Unstructured meshes also offer the possibility to initialize meshes with triangular cells or hybrid meshes which consists of quadratic and triangular cells. This kind of mesh type offered a solution to a problem which appeared after numerous simulations during the reduction of height of the diffuser h_v.
It turned out that due to a decreasing height of the diffuser h_v the angle of aperture at the end of the diffuser (Figure 4-3) becomes acuter. When the quotient h_v/D<1/3 which corresponds to α < 33.7° the simulation stops converging. The reason here could be found in the deformation of the cells especially in the last third of the diffuser.
In order to solve this problem triangular cells should be introduced to the diffuser area. This cell type is more robust against stretching and meshes with this feature converge also with h_v/D < 1/3.

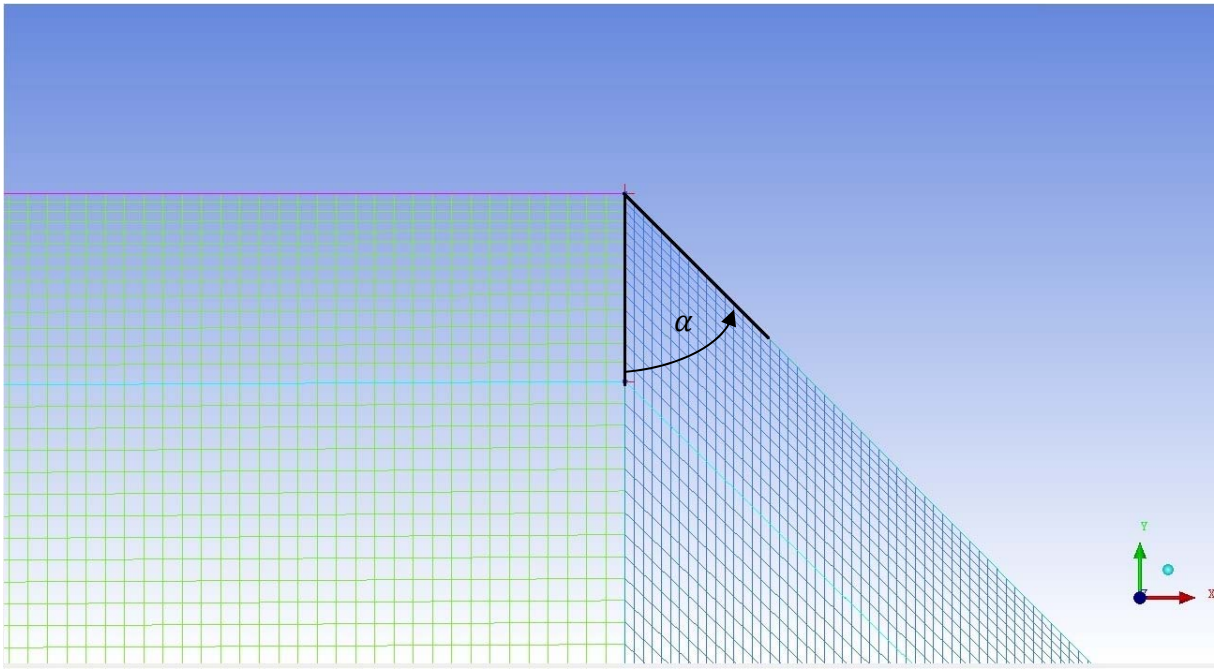

Figure 4-3 : angle of aperture at the end of the diffuser

Another important part of each mesh is the boundary layer. As it depends on the flow velocity and the geometry of the storage, it is different in almost every simulation and has to be adapted. On the one hand it must fulfill the requirements of the wall function, which means $y^+ > 30$. On the other hand it should match to the adjoining mesh density and go with the physical characteristics. Due to this balancing act the numbers of cells in the boundary layer and the spacing will be adapted in each mesh.

4.3 The aim of equal distribution

To use a thermal storage composed of a packed bed to full capacity, an equal distribution of the fluid flow is essential. Due to the little connection points of the particles and their relatively low thermal conductivity, it can be assumed that the heat transfer between the particles in the porous media is very slow or negligible and the heat is almost only transferred from the fluid to the solid. In the case of a bad flow distribution there are zones in the outer region of the storage bed which would heat slower than in the center.

However, there exists a mechanism that counteracts a heterogeneous temperature distribution. To be precise, in a heated region the mass flow rate through it decreases so that the flow of hot air is directed to colder regions which begin to heat up on their part. This effect is caused by the relationship between the temperature and the viscosity of the air which increases with higher temperatures. For this reason an

equal distribution is achieved faster than it would be the case of a flow of cold air. After a certain depth in the packed bed the equal distribution occurs in any case.
Taking this knowledge into account, the regions which can be exploited better with an optimized flow distribution are pointed out in Figure 4-4.

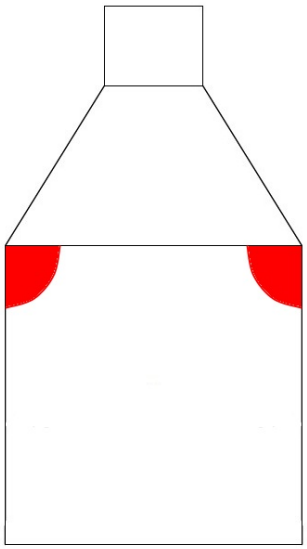

Figure 4-4 : untapped potential of a heat storage

There are methods for equal distribution like perforated plates or inlets with opposing flows which can effect a good flow distribution, but due to the high gas temperatures with related material problems, in this thesis this kind of built-in components will not be investigated.
So the diffuser geometry is the only feature which affects the fluid flow distribution. Besides the flow can be influenced by utilizing the pressure losses in the storage core which also depends on the storage geometry.

4.3.1 Characteristics of flow distribution

A possibility to characterize the flow distribution in a porous media within a thermal storage is the variable β, which was defined by Hansen [38]. This characteristic was developed for the Cowper stove and the variables in the formula are directly matching to this special problem. β can be calculated with the pressure drop Δp of the air passing through the porous media, the fluid velocity in the combustion chamber v_B and the mass flow $\dot{m}_A$.

$$\beta = \frac{2 \cdot \Delta p}{\rho_f \cdot v_B^2} = \frac{2 \cdot \Delta p}{\dot{m}_A \cdot v_B} \qquad \text{eq. 4-5}$$

The use of the fluid velocity in the combustion chamber v_B is problematic because in the considered case this parameter cannot be determined. For the utilization of the β-factor this velocity would have to be substituted and evaluated.
Another possibility to evaluate the flow distribution in porous media is used in the automotive industry for the design of catalyst beds in the exhaust system of motor vehicles. To calculate the uniform distribution index γ_A the physical velocity $|\vec{v}|$ and perfused area A_{total} is needed, given that $0 < \gamma_A < 1$.

$$\gamma_A = 1 - \frac{1}{2 \cdot \bar{v}_A \cdot A_{total}} \cdot \int_{A_{total}} ||\vec{v}| - \bar{v}_A \, |dA \quad \text{with} \quad \bar{v}_A = \frac{1}{A_{total}} \cdot \int_{A_{total}} |\vec{v}| dA \qquad \text{eq. 4-6}$$

A value of $\gamma_A = 1$ means a totally equal flow distribution while $\gamma_A = 0$ would mean, that the whole mass flow passes to one point in the area perpendicular to the flow direction.
All in all this parameter offers good characteristics especially because the needed variables for the calculation of γ can be extruded directly from the simulation results and the value of γ can be displayed intermediately in the data interpretation software. Therefore it should be used during the following explanations to quantify the flow distribution. From now on it is simply called γ or Gamma.

4.3.2 Flow distribution in an example geometry

For visualization reasons following streamline flow pattern will be shown in this subchapter. Moreover Figure 4-5 gives a good impression how the fluid flow behaves inside the storage.
The fluid flows enters at the inlet on the right hand side with 25 m/s. It can be seen that a large circular eddy forms in the outer region of the first two thirds of the flow distributor. This vortex ring surrounds the high fluid velocity gas in the inlet tube until the middle of the diffuser. For this reason it stays compact and conserves its high velocity. Close to the porous region in the last third of the diffuser the flow begins to split and to distribute over the full diameter of the diffuser. At the entry to the porous zone the fluid flow accelerates. This phenomenon can be explained with the displacement of the particles leading to a higher physical velocity in the porous region.

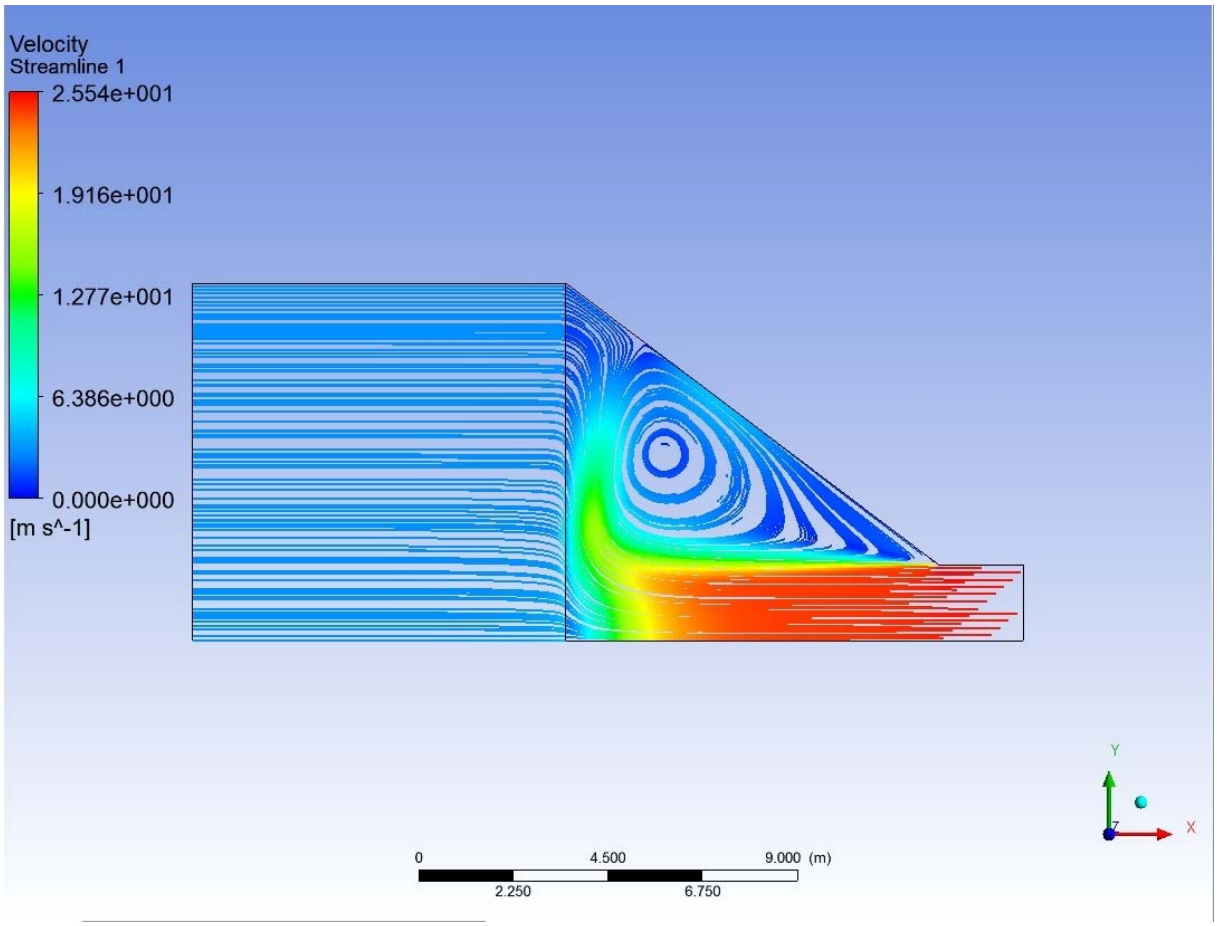

Figure 4-5 : streamline flow pattern of an example storage geometry

The flow pattern is constant for different heights of the diffuser h_v and storage diameters. Only in some extreme case scenarios the eddy disappears.

4.4 Verifying the mesh independence

The mesh independence study is a very important part of every simulation process. A lot of effort has to be invested on this topic to guarantee the correctness of the whole thesis. The study has to prove if the mesh density fulfills two requirements. First a grid has to be found whose flow profile does not change during a refinement. Secondly, this grid has to be coarsen until the profile changes again. Theoretically, with this method one achieves a mesh which is fine enough for a correct computation but so coarse that no computation time is wasted.

In reality the selected mesh may differ from this theoretical concept. If the mesh density is higher than needed, the results are still correct. As we are searching for an example mesh density which should be transferable to other geometries, we should take a confidence coefficient into account to ensure the correctness of the following simulations with varying geometries.

4.4.1 Mesh with quadratic cells

Figure 4-6 provides an overview of the investigated cross section and the organization of the mesh independence study. For the investigation, the full cross section of the storage geometry was calculated, later it could be proven that the flow profile in every point for a reduced cross section geometry is exactly the same as the flow profile of the entire section. The dimensions of the storage are similar to existing projects to create realistic conditions. In order to generate maximal turbulences, the flow conditions of a full load case were selected. Both are summarized in table 4-1.

table 4-1: Test preconditions

Parameters of a heat storage	*Preconditions values*
Storage diameter D	$17.0m$
Storage height H	$17.7m$
Diffuser height h_v	$8.85m$
Inlet diameter d_{in}	$3.6m$
Diffuser quotient h_v/D	$1/2$
Mass flow rate $\dot{m}$	$104.902kg/s$
Temperature T_{in}	$849.15K$
Euler number Eu	$936{,}4$
Velocity at inlet v_{in}	$\sim 25m/s$
Pressure drop Δp	$\sim 3570\ Pa$

First the storage geometry is split into different domains from A to E. As the domains D and E are not relevant for the following investigation the results for these parts will not be presented. The numbers on the top of the drawing represent some of the investigation lines where the flow profile was examined. The most interesting is investigation line 3, here the fluid enters the porous zone and at this position later the Gamma value will be measured. Therefore it is important that the flow profiles at this line become independent of the mesh. For a complete analysis of the mesh independence, the flow profile comparisons in front and behind this line were performed extensively.

The numbers below and on the left hand side of the model in Figure 4-6 represent the quantity of cells on each vertex for an example test case. These values should be varied until the optimum is found.

Only for the number of cells in the boundary layer there cannot be found an optimum this way, since the thickness of the boundary layer is dependent of the flow

characteristics and of the number of cells on the other vertical vertex. Moreover the height of the nearest cell to the wall is fix due to a constant y^+-value. As a result, the number of cells in the boundary layer has to be adapted in each case for the variation study.

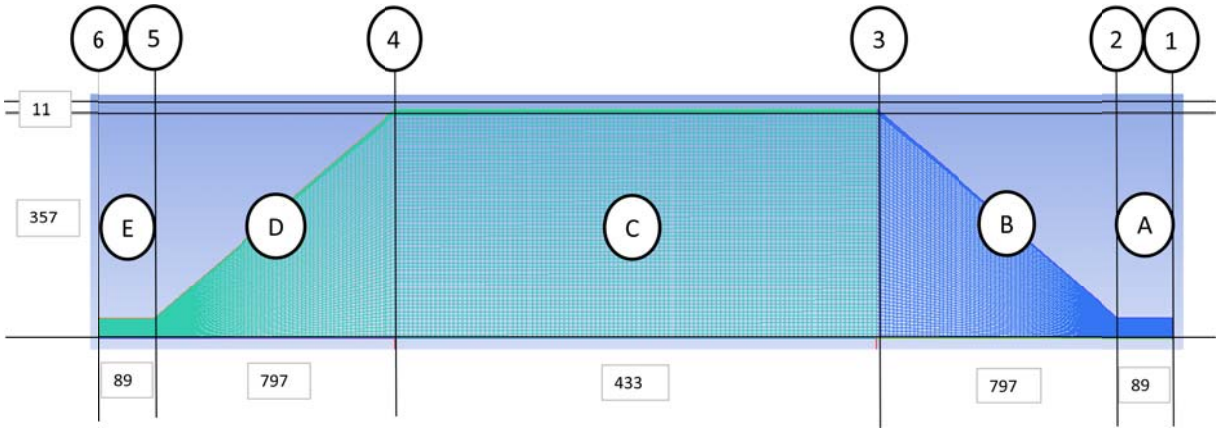

Figure 4-6 : Overview: mesh independence

In the next step, the numbers of cells are varied for each test case and the flow profiles on the investigation lines were compared. Thus, eleven test cases with different mesh densities were formulated. For some domains not every test case is tabulated because the solution could be fixed during the process. For example table 4-2 illustrates the tested mesh densities in the inlet region and the vertical vertex only for the first seven tests. Owing to the large number of flow profile diagrams, their low quality and confusing appearance, they are not suitable for an illustration in this thesis. So they will not be shown in this chapter, instead tables with the numbers of cells on the vertexes and flow distribution parameters will be quoted.

table 4-2 : mesh density in domain A

	Test1	*Test2*	*Test3*	*Test3b*	*Test4*	*Test5*	*Test6*
number of cells in A	89	133	89	89	265	89	89
number of cells vertical	179	179	179	179	179	119	119

Soon it could be found that the flow profiles in domain A and at the investigation line 3 are relatively independent of the number of cells in domain A. It could be shown that the minimum of 89 cells is sufficient.

The number of cells on the vertical vertex has been varied simultaneously. It could be found that the number of vertical cells influences the flow profile near the symmetry axis at several investigation lines. This phenomenon disappears for 179 cells on the

vertical vertex. So this number of cells appeared to be sufficient for the flow profiles in the domains A and C.

The Gamma value is collected at the entry of the porous zone between the domains B and C. It is also here where the differences between the differing mesh densities and storage geometries can be seen best. As the domain C lies on the downstream side of this investigation line, the mesh density in this sector does not influence the flow profile that much. The flow profiles on the downstream side of this border are even affected by the mesh density in domain B.
For those reasons and due to the experience of previous mesh independence studies with little different geometries and preconditions, in domain C only two different mesh densities were tested. The different densities only affect the flow profile in the region near the entry to the porous zone. After some distance, about 50cm, the porous media produces an equal flow distribution independent of the number of cells.

table 4-3 : mesh density in domain C

	Test1	*Test2*	*Test3*	*Test3b*	*Test4*	*Test5*	*Test6*
number of cells in C	433	649	433	433	649	433	433
number of cells vertical	179	179	179	179	179	119	119

These conclusions come out of the first seven tests presented in table 4-3. In these tests it could be figured out that the variation of the mesh density in domain B influences the flow profile in the critical region of C, independent of the numbers of cells in C. Beyond this region, the flow profiles are independent of the number of cells in any case. Therefore it could be chosen the lower mesh density.

The most critical domain is the flow distributor (domain B), here the cells are stretched by the geometry. Also the large eddy which can be seen in Figure 4-5 is placed in this region and there must be an adequate mesh to calculate it correctly.
The mesh density in the flow distributor is constituted by the numbers of cells in B and on the vertical vertex. It could be found that in domain B the numbers of cells on the vertical vertex which were enough for the other domains are not enough in this region. An increasing of the numbers of cells of the vertical vertex leads to small differences in domain B and to constant flow profiles in the other regions. So a number of 357 cells has been chosen.

table 4-4 : mesh density in the domain B

	Test3b	*Test4*	*Test5*	*Test6*	*Test7*	*Test8*	*Test9*	*Test10*
cells vertical	179	179	119	119	179	179	357	357
cells in B	797	531	237	531	1196	1794	797	1196
cells in C	433	649	433	433	433	433	433	433

From the data in table 4-4 it is apparent that the searching process for the numbers of cells in B was the hardest. Several mesh densities in domain B were tested, very low densities for Test5 and very high densities for Test8. Both do not return correct results, while low densities effect imprecise results, very high numbers of cells lead to numerical problems and oscillations in the flow profiles. The other meshes with 531, 797 and 1196 cells in domain B result in very similar flow profiles.

table 4-5 : Comparison of the Gamma values of the most promising meshes

	Test3b	*Test4*	*Test7*	*Test9*	*Test10*
cells vertical	179	179	179	357	357
cells in B	797	531	1196	797	1196
cells in C	433	649	433	433	433
Gamma	0.9612	0.9611	0.9599	0.9625	0.9623
Discrepancy to Test9	0.13%	0.14%	0.26%	0.00%	0.01%

table 4-5 illustrates the remaining meshes with their Gamma value. Due to the almost identical flow profiles of these meshes, a comparison of the Gamma value is permitted and reasonable. The influence of the number of cells on the vertical vertex can be illustrated by the comparison of the Gamma values of Test3b and Test9. Also the marginal differences between Test3b and Test4 as well as between Test9 and Test10 caused by the disparity of cells in domain B can be observed.
Finally the mesh of Test9 was selected, a discrepancy of Gamma of 0.01% legitimates the decision for the coarser grid.

4.4.2 Hybrid meshes

As already explained in chapter 4.2.4, hybrid meshes offer the possibility to analyze the flow distribution for geometries which do not converge with quadratic cell meshes, especially for h_v/D < 1/3. It is considered that the results of the quadratic cell meshes deliver the most exact results. Therefore, for the usage of the hybrid meshes

it must be proven that they produce flow profiles which are comparable to the quadratic cell mesh profiles.
For this reason, a flow profile near the entry to the porous zone of the in chapter 4.4.1 selected quadratic cell grid with example flow condition was compared to different hybrid meshes. The aim of these experiments was to find an equivalent hybrid mesh. So nine hybrid meshes with different mesh densities and blocking strategies were developed.
But the comparison of their flow profiles leads to a disappointing result. The flow profiles of all hybrid grids differ at many points. The curves cross the reference curve at many positions and the curve progression of each curve differs significantly. As a result no matching hybrid mesh could be found and meshes with h_v/D < 1/3 cannot be compared to the others.
Consequently this leads to limitation of the scope, because there is no possibility for the investigation of storage geometries with h_v/D < 1/3.

4.5 Automation of the mesh generating process

The used software, ICEM and FLUENT, offer the possibility to record scripts to replay the steps done by the user. With the recorded file e.g. one can regenerate the mesh and storage geometry or redo steps until a chosen point and complete the mesh generation process in a different way. With this method, similar geometries can be generated. The advantages of the replay function are obvious. With this option, it is possible to analyze more geometry variations, thus obtaining more information on the critical design parameters, which is part of the conceptual formulation. This can yield optimal design recommendations within the project time limits, which matches with one of the goals of this thesis.
Since the form of the geometry is the same and only the dimensions vary, these parameters can be substituted with run-time variables. Also the input parameters for the solver setting can be substituted this way. So every variable presented in chapter 4.1.1 is parameterized in the used script. In order to accelerate the process and to reduce redundancies, it was necessary to merge the two replay files into one script which controls the whole process. This was done especially because some variables are needed for both processes, e.g. the inlet diameter which corresponds to the hydraulic diameter in the solver settings. For this reason the replay files were generated using Windows Powershell. With this tool it is possible to create two replay files that can be imported directly into the two programs so that no more manual adjustments are required. The header of an exemplary script can be reviewed in the appendix.

At the same time different input parameters need different mesh properties. The settings for the boundary layer like spacing and its thickness can be adjusted in the script. But after the creating process, it must be controlled if the mesh density in the boundary layer matches to the rest of the mesh. It is not tolerable that the last row of the boundary layer cells is larger than the connecting cells in the main body. In an ideal mesh these cells would have the same size.

The mesh independence study suggests one mesh for the tested geometry. Hence it can be derived a mesh density which is applied to other geometries and has to be conserved to get comparable results for the different geometries. This adaption cannot be done automatically so that the mesh density is adapted manually. Thanks to the confidence coefficient, test even suggested that divergences in the mesh density of approximate 10% only lead to a negligible discrepancy of the γ value.

All in all this scripting process made it possible to review such large amount of geometries within a short period of time and it is the most important part of the solution concept.

5 Presentation of the simulation results

The aim of this chapter is to present the results of the simulations and to draw some conclusions from them. The chapter has been divided into two sections. In the first part the dependence between different parameters is identified by plotting them into ceteris paribus diagrams. With these diagrams it is possible to find the parameters which most influence the flow distribution inside the storage.
In the next step all simulation results have been recycled and integrated into one diagram which is based on the Ψ-Reynolds correlation. This approach will be presented in detail later and is well-suited to identify correlations between the flow distribution and the geometry parameters. Of course this approach has to be validated to achieve significant results.

5.1 The influence of the parameters

One main goal of this thesis is to identify how the flow distribution is affected by the variation of each parameter of the storage system. For the comparison of a large amount of measuring points, diagrams are very useful tools. For this reason in this chapter, five ceteris paribus diagrams are presented. Each graph offers the possibility to identify trends for two storage characteristics.
Every plot consists of a vertical axis which represents the flow distribution γ, a horizontal axis which scales the first varied parameter and three curves. Each curve represents one constant value for the second varied parameter. As a result within one curve only the parameter is varied which represents the horizontal axis, everything else remains the same.
The comparison of the three curves and the curve progression allow conclusions on the influence on the flow distribution of both parameters. For instance it can be seen which parameter influences the flow distribution more or how the parameters influence each other.

5.1.1 Defining the limits

First of all it must be discussed in what range the parameters of the storage geometry should be varied. Some selected limits have physical reasons, for example, an increasing velocity in the incoming tube leads to an increasing friction and pressure drop. Velocities higher than 30m/s reduce the efficiency of the storage system

significantly. This requirement limits the mass flow rate for small inlet diameters. The mass flow rate of other storage geometries with larger inlet diameters is, similarly to temperature, constricted by the possible surrounding systems, for example by the maximal production of hot air. The lower limit of the mass flow rate can be seen in a analogous context, because a storage that needs too long for charging and discharging is also neither efficient nor economical. But as part load case scenarios should also be considered, a small value for this lower limit was selected.
Other parameters are limited by economical reasons, like the diffuser quotient or the storage height. Especially the flow distributor which is per definition an empty space and cannot be used for the containment of storage material and therefore it should be as small as possible to reduce the costs of the container.
Taking into account all these factors, the discussions with storage design experts led to the values listed in table 5-1.

table 5-1 : extreme values for the storage geometry

	lower limit	*upper limit*
Storage diameter D	$6m$	$20m$
Inlet diameter d_{in}	$1m$	$4m$***
Inlet velocity v_{in}	-**	$30m/s$
Mass flow rate $\dot{m}$	$26.226kg/s$	$104.9\ kg/s$
Diffuser quotient h_v/D	$1/3$*	$1/2$
Temperature T_{in}	$773.15K$	$1073.15K$
Euler number Eu	600	-

* The limit of 1/3 is no design criteria but a mesh criteria mentioned in chapter 4.2.4

** There is no lower limit for the inlet velocity but there is one for the mass flow rate; therefore it can be calculated a lower limit regarding the upper limit for the inlet diameter

*** The largest tubes are offered with a diameter up to three meters. For larger inlet diameters, tube bundles consisting of a lot of smaller tubes have to be used.

In order to map the greatest possible range, the extreme values should appear in the ceteris paribus diagrams. Besides, regular intervals between the five points of one curve are necessary to get comparable curves as well as a complete analysis of the reviewed parameter field. On the other hand this procedure leads to a possible problem because some values lie a bit outside of the defined range. That is not that problematic since the aim of this simulation is to identify the influences of the different parameters and to observe the resulting trends of the curves.
Only the value of the Euler number must not go below its limit, otherwise the simulation results become invalid. In order to avoid this, the parameter H which does

not appear in table 5-1 but influences the Euler number is used as an regulatory instrument. If the Euler number is greater than 600, it is equal to the storage diameter D. Only in some extreme case scenarios, if the Euler number tends to fall under the limit, H will be adjusted to prevent this.

Since some of the variables must have a constant value in the ceteris paribus diagrams they should be chosen in a intelligent way. In order to get the less influenced results, for the constant flow parameters like temperature and mass flow rate, the arithmetic mean of the extreme values is used. The constant geometry dimensions have been chosen dependent on their Psi and Re values to achieve a spreading over the parameter field which is introduced later.

The largest tubes are offered with a diameter up to three meters. For larger inlet diameters, tube bundles consisting of a lot of smaller tubes have to be used.

5.1.2 Storage diameter variation

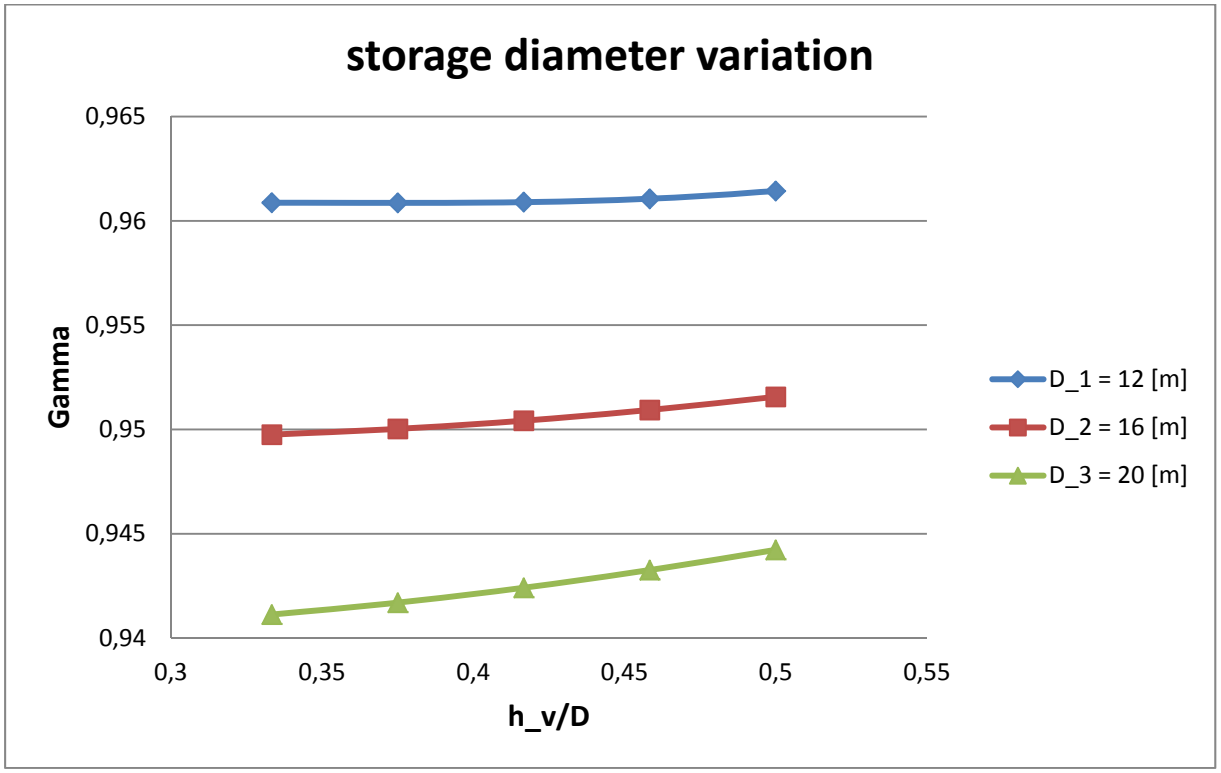

Figure 5-1 : storage diameter variation

table 5-2 : constant values for the storage diameter variation

$T_{in}[K]$	$d_{in}[m]$	$\dot{m}\ [kg/s]$
923.15	3	65.5635

The first conclusion that can be identified in Figure 5-1 is that the storage diameter D influences the gamma factor considerably more the then h_V/D quotient. A smaller storage diameter results in a significantly better flow distribution. In interpreting these findings, we have to take into account that the inlet diameter is constant and the quotient d_{in}/D increases. Since the diameter of the jet of hot air remains constant over a long distance, (Figure 4-5) it is easier for the flow to distribute in a smaller geometry with a smaller storage diameter and with a relatively larger inlet diameter. As we will see later, this trend continues for decreasing storage diameters, the best values for Gamma can be achieved with the smallest values for D when the vortex ring disappears (not shown in the diagram). Furthermore one can see that a better h_V/D ratio leads to a bit better flow distribution. This effect increases with a larger storage diameter. So it can be assumed that γ depends more on h_v than on the quotient h_v/D.

5.1.3 Diffuser quotient variation

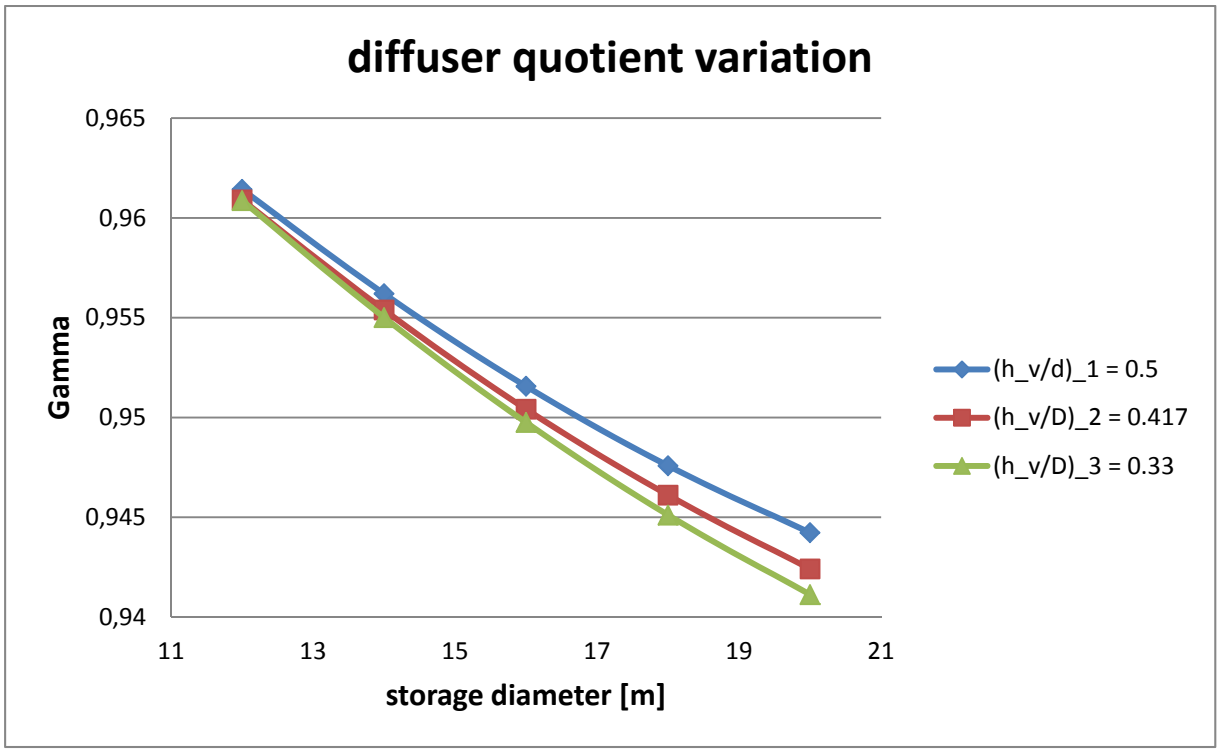

Figure 5-2 : diffuser quotient variation

table 5-3 : constant values for the diffuser quotient variation

$T_{in}[K]$	$d_{in}[m]$	$\dot{m}\ [kg/s]$
923.15	3	65.5635

In this diagram (Figure 5-2) some values of the previous diagram could be used. So it also serves for the validation of the conclusions of the first diagram. Likewise the first diagram, (Figure 5-1) one can see the decreasing flow distribution with a larger storage diameter for different h_V/D values. Moreover the differences between the three curves increase with an increasing storage diameter. This is caused by the same effect which could already be observed in Figure 5-1 referring to the increasing inclination of the curves with a higher storage diameters. Consequently the best flow distribution for a given storage diameter can be achieved with the biggest allowed diffuser height. It also can be assumed that the larger the storage is, the more profitable are the volume and height of the diffuser.

At this point it is important to mention that the cost of flow distributors raise with their volume. For that reason it must be found an economic compromise between the advantages of a better flow distribution and the increasing costs of the whole storage system.

5.1.4 Inlet temperature variation

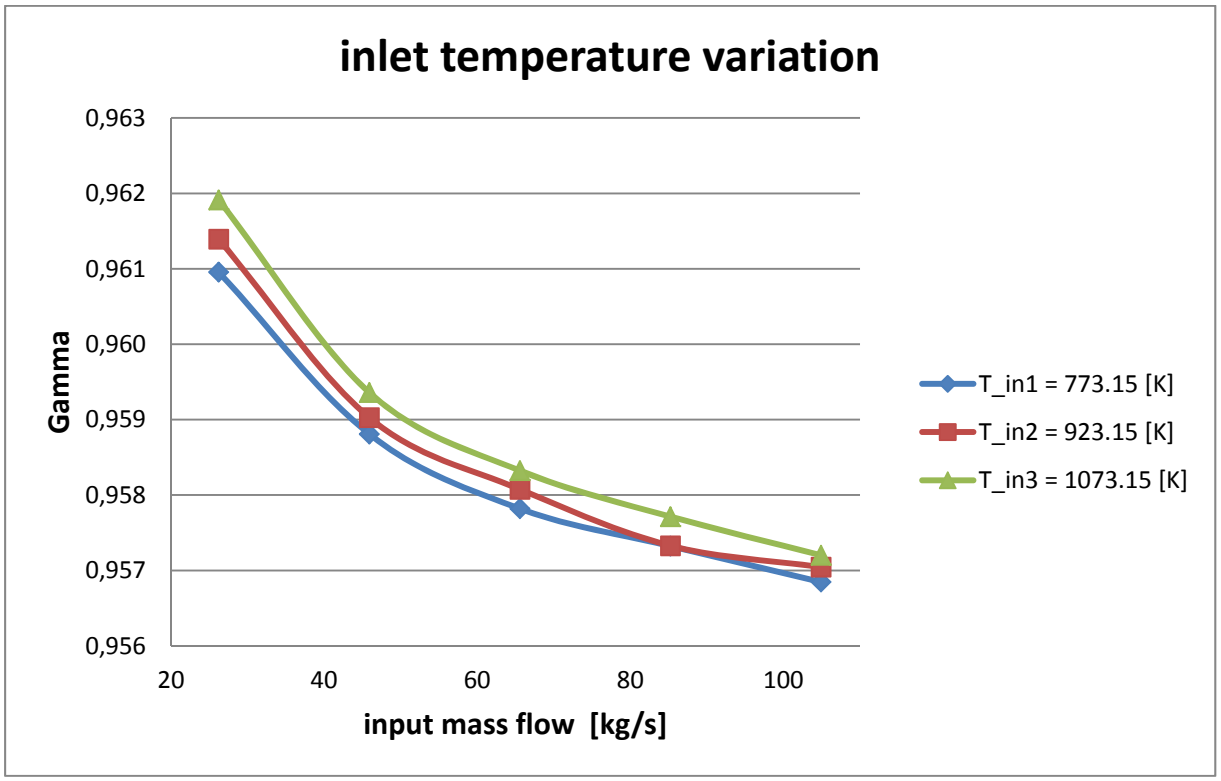

Figure 5-3 : inlet temperature variation

table 5-4 : constant values for the inlet temperature variation

$d_{in}[m]$	$D[m]$	h_v/D
3.7	20	0.33

Another parameter which should be varied is the temperature. It affects the fluids density and viscosity, for this reason it influences the flow characteristics. However, it can be supposed that its influence on the flow distribution is slight.

As it can be seen from the line graph this assumption can be proved because the scale on the vertical axis shows a very small interval, which means that the differences are also very small. A difference of 0.001 for the γ value means that the effect of the temperature variation is within the range of numerical inaccuracy. This also explains why the fourth point of T_{in2} differs from the expected position. Nevertheless the other points are in the expected positions and the curves do not intersect each other. This underlines the quality of the selected grid and the simulation results.

However it is astonishing how the influence of the mass flow rate on the flow distribution is also little. In this selected geometry the difference of Gamma between the highest and lowest mass flow rates is only 0.005. That also implies that both flow parameters have only a slight influence on the flow distribution.

Furthermore several conclusions may be drawn from the graph. First, a low input mass flow leads to a better flow distribution. As the velocity and the mass flow rate are linked, this conclusion is directly connected to the results of 5.1.5. In the inlet temperature variation diagram the differences are more visible because the scale of the γ axis is a lot finer.

Second, it can be seen that a higher temperature has a positive impact on the flow distribution. Both conclusions can be extracted from the simulation results but its influence is marginal compared with the effect of other parameters, specially the diffuser dimensions.

5.1.5 Inlet velocity variation

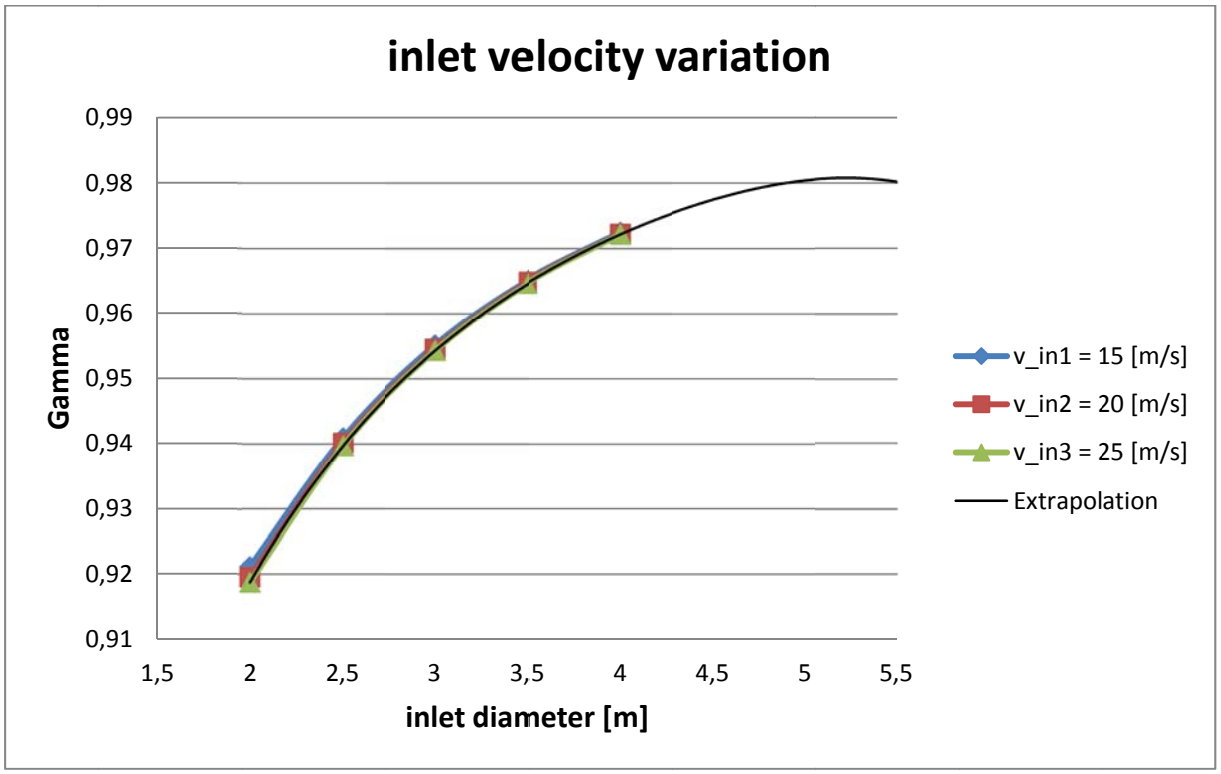

Figure 5-4: inlet velocity variation

table 5-5 : constant values for the inlet velocity variation

$T_{in}[K]$	$D[m]$	h_v/D
923.15	15	0.5

The graph shows a steady increasing quality of the flow distribution with an increasing inlet diameter. This variable has a big impact on the flow distribution. The reason for this effect may be found in a increasing mass flow rate which results of this configuration with increasing inlet diameters. A high mass flow rate leads to a higher velocity in the packed bed, and therefore to a higher pressure drop and Euler numbers.

The curve's geometry suggests that it has an asymptote. The extrapolated trendline which was added to the diagram confirms the assumption and returns a value of about γ = 0.98 for the horizontal asymptote of the flow distribution in this configuration. In order to reach this value, an inlet diameter of more than 5 meters would be necessary.

Since the inlet diameter has so much influence on the flow distribution, it seems that the velocity at the inlet does not have much influence on the γ value. In fact the

differences between the curves are comparable with theFigure 5-3 : inlet temperature variation diagram (Figure 5-3). So it can be recognized that a higher velocity leads to a worse flow distribution. This effect decreases with an increasing inlet diameter.
In the observed range of values for the inlet diameters, it was not possible to show lower velocities because the lower limit of the mass flow rate leads to the minimal velocity for this diagram. In the case of the largest inlet diameters the mass flow rate already falls below these minimal values. In the next diagram (Figure 5-5) a similar correlation is presented to validate the conclusions from this diagram and to show that the identified correlations are also valid for different storage geometries.

5.1.6 Mass flow rate variation

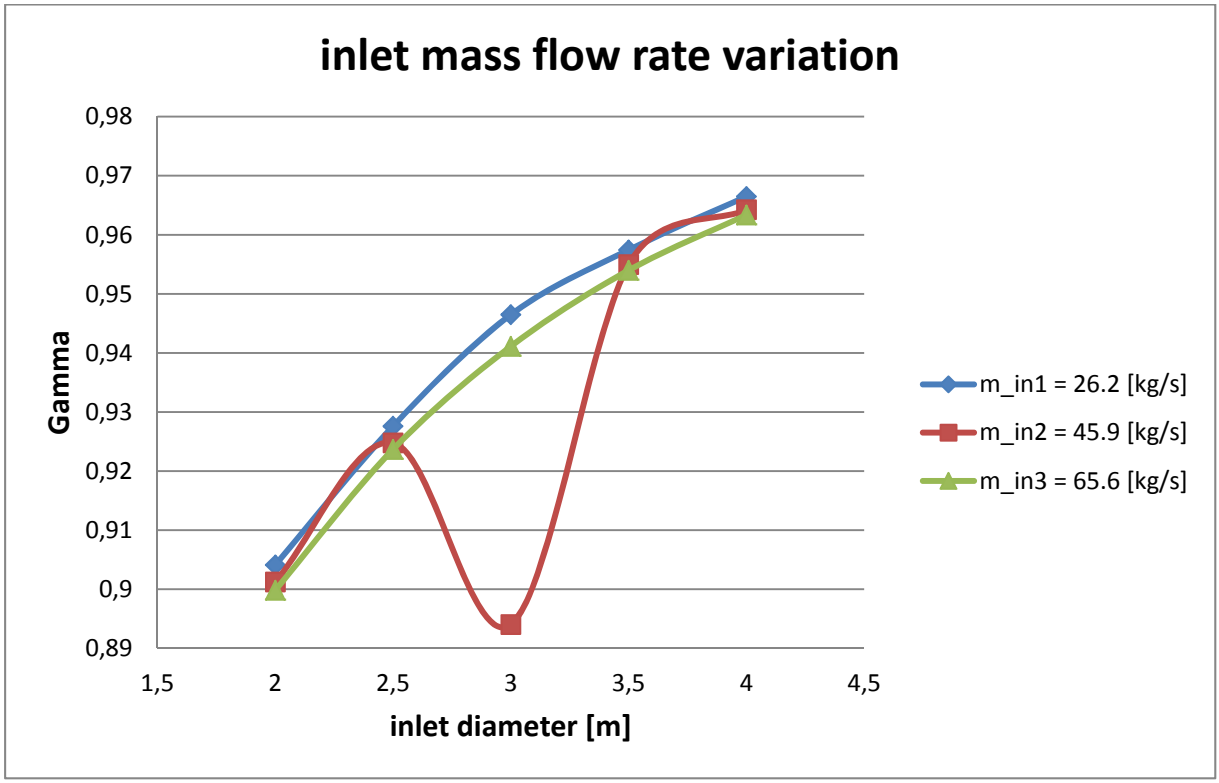

Figure 5-5 : mass flow rate variation

table 5-6 : constant values for the mass flow rate variation

$T_{in}[K]$	$D[m]$	h_v/D
923.15	20	0.33

This diagram is similar to diagram Figure 5-4, it even uses the same axis labels. The main difference between the two graphs is that, in this case, the mass flow rate is

used which is independent of the inlet diameter in contrast to the inlet velocity. That is the reason for the constant distance between the curves.
In both cases the vertical axis has a wide range which proves that the inlet diameter has a significant impact on the flow distribution. It can also be seen that the trend for the γ value with an increasing inlet diameter remains the same also in case of a different storage geometry (compare table 5-5 and table 5-6). Furthermore it could be shown that analogue to the velocity, a higher mass flow rate leads to a worse flow distribution. Also the curves in this diagram have a larger distance between each other then in diagram Figure 5-4. The reason for this may be found in differing storage and diffuser dimensions.
It has to be noticed that some of the extreme values in the diagram exceed the limits for the inlet velocity established in chapter 5.1.1. These values had to be used to get three stacked curves. The inlet velocity limit is also the reason for the chosen mass flow rates which are relatively low compared with the limits.
What catches one's eye is the third value of the m_{in2} curve. It could be proved that it is no error in the simulation; this was confirmed several times. Consequently it must be considered as a local anomaly at this point. With the Psi-Re correlation which will be discussed in the next subchapter, this assumption can be explained and finally proven.

5.2 The Ψ- Reynolds correlation

The objective of this subchapter is to unite all measurement points which were generated for the ceteris paribus diagrams into one diagram. For this reason the parameters Re and Ψ were introduced in chapter 4.1.2. The Reynolds number describes the flow characteristics and Ψ merges the geometry parameters. Every possible storage geometry and flow variation can be expressed with these dimensionless parameters and consequently the variations become comparable in a two dimensional parameter field. Furthermore, the Ψ- Reynolds correlation implicates that the flow distribution is constant for different geometries with the same values for Re and Ψ.
First of all, it must be validated if this simplification is allowed by testing the implications of the Ψ- Reynolds correlation. In the second step, the resulting diagram can be presented and interpreted.

5.2.1 Validation

Figure 5-6 introduces the Ψ- Reynolds diagram and presents the survey area. The blue dots are the extreme values calculated with the equations eq. 4-3 and eq. 4-4 and the extreme values defined in 5.1.1. Therefore the area encased by the black lines is the complete area of investigation. It is not possible to create a geometry within the defined limits of table 5-1 which lies outside this area. Consequently most of the values of the ceteris paribus diagrams are also located within these borders. On the contrary it is possible to create geometries which lie inside this area and violate the defined limits.

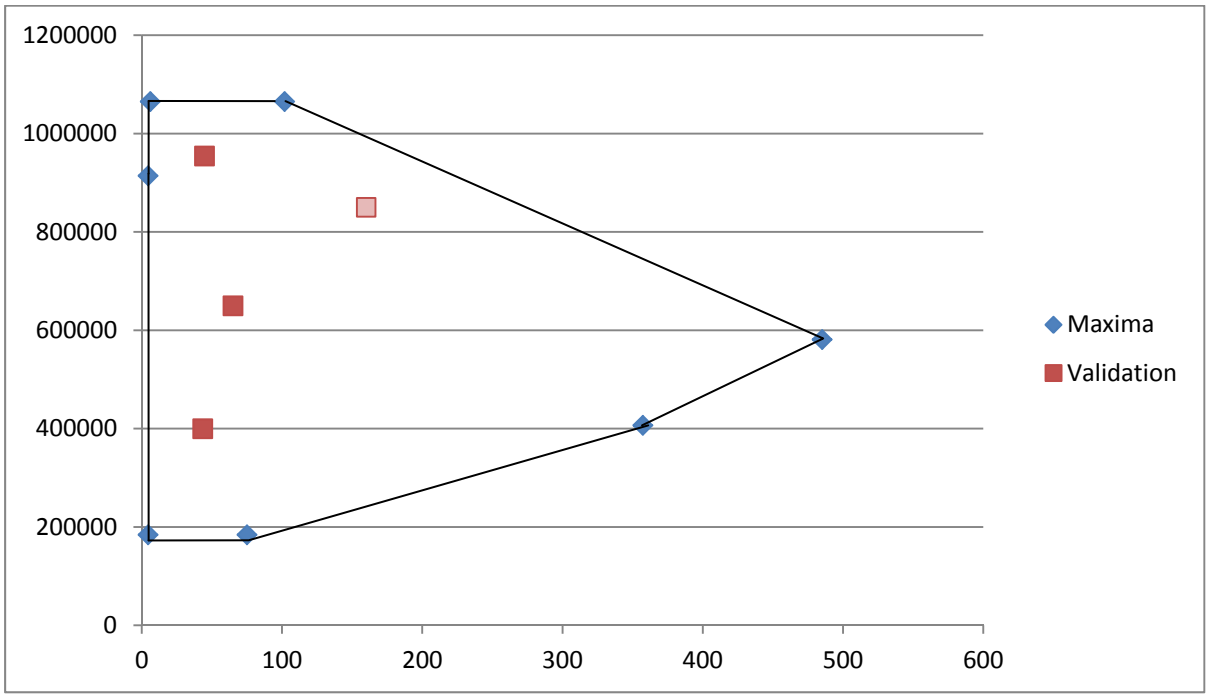

Figure 5-6 : area of investigation including the validation points

As the dimensionless parameters depend on various geometry and flow parameters, it is possible to create several storage geometries which have the same value for Re and Ψ. Following the Ψ- Reynolds correlation they must have the same value for the flow distribution.

For the validation some points within the survey area were investigated. It must be checked if the γ value is constant for different geometry and flow configurations with the same values for Re and Ψ. This was done for four points within the investigation area which are marked with red dots in Figure 5-6. The dot with a lighter red represents a geometry which was simulated with a hybrid mesh. This was done to test the universality of the Ψ- Reynolds correlation.

In interpreting these findings, we have to take into account that these are simulation results which only represent reality and therefore small variances are normal and part of every simulation process. Especially if a lot of parameters are changed, like it is necessary in this case. For that reason a relative discrepancy of 1% to an average value should be considered as tolerable.

table 5-7 : data for a validation point (Re=400000, Ψ=43.4)

variations	*m[kg/s]*	*T_in[K]*	*d_in [m]*	*D[m]*	*h_v/D*	*Eu*	*Re*	*Ψ*	*γ*	*Discrepancy*
A	50.0	1033.08	3.6	15.0	0.40	804	400000	43.4	0.974	0.01%
B	50.0	933.08	3.8	17.0	0.45	933	400000	43.4	0.974	0.06%
C	50.0	883.08	4.0	15.1	0.33	803	400000	43.4	0.978	0.45%
D	53.1	970.44	4.0	16.0	0.37	864	400000	43.4	0.977	0.32%
E	48.2	1073.15	3.4	14.4	0.42	770	400000	43.4	0.972	-0.20%
F	45.0	1073.15	3.2	14.8	0.51	804	400000	43.4	0.968	-0.58%
G	45.0	959.56	3.4	13.6	0.37	717	400000	43.4	0.973	-0.06%
	Average γ: 0.97364014									

table 5-8 : data for a validation point (Re=650000, Ψ=65)

variations	*m[kg/s]*	*T_in[K]*	*d_in [m]*	*D[m]*	*h_v/D*	*Eu*	*Re*	*Ψ*	*γ*	*Discrepancy*
A	68.8	802.38	3.6	17.2	0.35	899	650000	65	0.969	0.39%
B	73.1	1001.09	3.3	16.2	0.37	847	650000	65	0.966	0.07%
C	60.0	900.00	2.9	14.9	0.40	775	650000	65	0.960	-0.46%
	Average γ: 0.964953									

table 5-9 : data for the validation point (Re=954392, Ψ=44.6)

variations	*m[kg/s]*	*T_in[K]*	*d_in [m]*	*D[m]*	*h_v/D*	*Eu*	*Re*	*Ψ*	*γ*	*Discrepancy*
A	104.9	849.15	3.6	17	0.5	936	954392	44.6	0.972	-0.03%
B	104.0	773.15	3.8	16.1	0.4	805	954392	44.6	0.973	0.08%
C	96.80	820	3.4	13.4	0.35	665	954392	44.6	0.972	-0.05%
	Average γ: 0.972536									

table 5-10 : data for the validation point (Re=850000, Ψ=160)

variations	*m[kg/s]*	*T_in[K]*	*d_in [m]*	*D[m]*	*h_v/D*	*Eu*	*Re*	*Ψ*	*γ*	*Discrepancy*
A	90.1	876.5	3.4	19.2	0.20	1009	850000	160	0.973	0.10%
B	101.7	926.5	3.7	20	0.18	1049	850000	160	0.971	-0.04%
C	78.0	773.6	3.2	18.2	0.20	947	850000	160	0.971	-0.05%
	Average γ: 0.97200733									

For the demonstration of the results these four cases should be presented. The data in table 5-7, table 5-8, table 5-9 and table 5-10 show the varied geometry and flow parameters of different test cases. It also can be seen, that the parameters were varied within the defined limits and regarding constant values for Re and Ψ. To make a definite statement at least three test cases with constant values for Re and Ψ should be investigated and reproduce similar Gamma values.
On the right hand side the values for γ and the discrepancy between the specific value and an average γ are illustrated. It can be seen that the discrepancies between the test cases are small. With a difference of 0.58% the value of variation F in table 5-7 varies most. All other variations show slighter discrepancies and support the assumption of the Ψ- Reynolds correlation and its universality. Consequently our validation criterion was not violated and the correlation is validated.

5.2.2 Integration into a three dimensional diagram

After the validation, it is possible to present all results of the study in a compact form. For this reason the two dimensional survey area which was presented in Figure 5-6 is extended by a third dimension. This accessory variable is γ and in the following diagrams, its dependency to the Reynolds number and the Ψ parameter can be observed. In order to improve clarity, these results should be presented in two different diagrams with the same statement.
The first diagram is three-dimensional which unfortunately can be shown in only one perspective. From the selected point of view some points which lie behind the plain are not observable. The distinctive form of the survey area (Figure 5-6) would be visible if we looked at the plain from above.
Every black dot in the diagram represents the simulation result for one geometry with its γ value. Most of these values were generated during the creation of the ceteris paribus diagrams. The extreme geometries at the corners of the diagram and some other geometry variations which close the gap between these dots were simulated later to get a more complete investigation of the survey area. The regions between the points are calculated by an interpolation function. This results in a bumpy plane which forms oblique in the three-dimensional space and can be seen in Figure 5-7. The red regions represent the geometries with the best flow distribution while the blue regions show the worst.
The best flow distribution of γ=0.996 is achieved for Ψ = 4.5 and Re = 914123. The following sharp drop of the γ values for decreasing Ψ values can be explained with the formation of the vortex ring for a specific d_{in}/D quotient. After this unavoidable

event the γ values decrease continuously for an increasing value of Ψ. Therefore the point with the worst flow distribution with the defined limits is also the point with the highest Ψ value, here γ is 0.875.

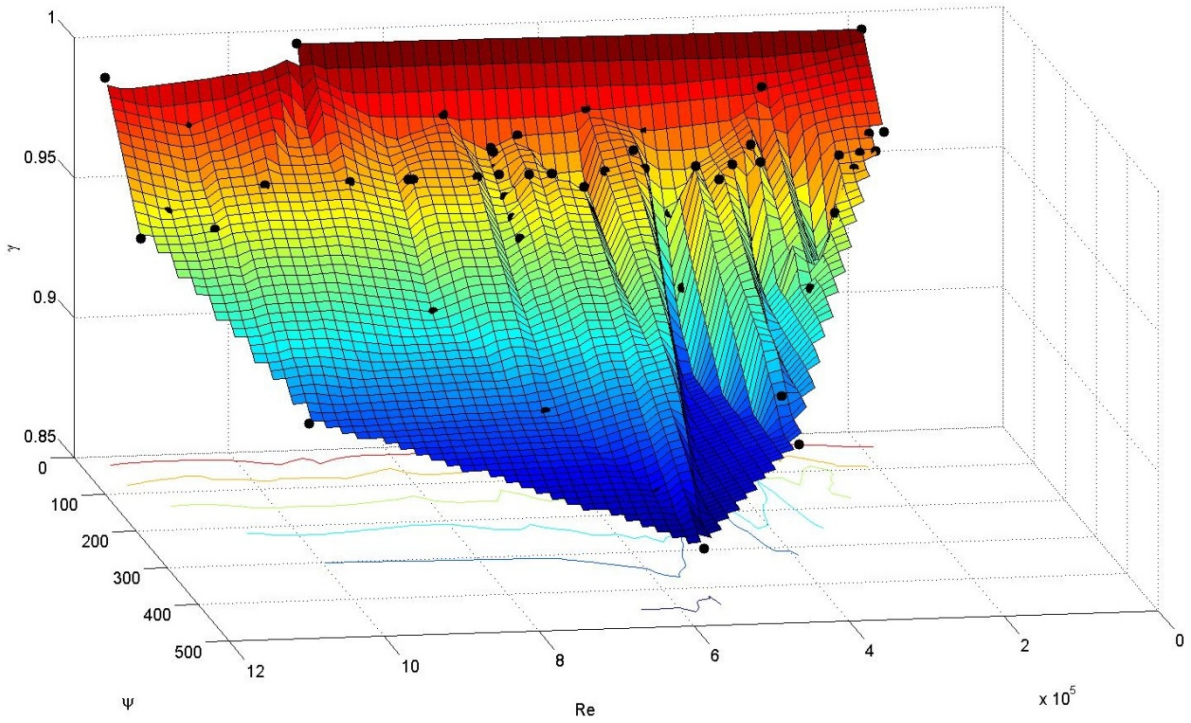

Figure 5-7 : three dimensional diagram of the complete survey area

The Re parameter has almost no general influence on the flow distribution which underlines the results of subchapter 5.1.4. It could be finally proven that the diffuser geometry has a significant higher impact on the γ value. That is not surprising as we could observe a high impact of the inlet diameter in diagram Figure 5-4 and Figure 5-5 as well as a high impact of the storage diameter in Figure 5-1 and Figure 5-2. Both parameters are part of the equation for the calculation of the parameter Ψ.

Besides these general statements the plane shows some unevenness which means that the value of γ fluctuates for similar values for Ψ and Re. Since there are numerical uncertainties and the area between the points is calculated with an interpolation formula, the small apexes may have no meaning. But it can be observed that the simulation results predict a local minimum for Re = $4.8 \cdot 10^5$. There are several points around and in this minimum which support this assumption. Some of them are lying behind the plane because the interpolation function could not capture them, for example the outlying point in Figure 5-5. So this minimum is affirmed by many simulations results.

The second diagram is a two dimensional contour graph. The contour lines connect points where the function has the same particular value. The gradient of the function

is always perpendicular to the contour lines. When the lines are close together the magnitude of the gradient is large: the variation is steep.

In Figure 5-8 the local minimum can be seen very clearly. It also becomes obvious that for Re > $6 \cdot 10^5$ the contour lines are almost parallel to the horizontal axis, while the area for lower Reynolds numbers is more fissured. That implicates an unstable flow pattern for part load cases.

Another declaration which can assumed from this figure is that the area with high γ values is wider in the lower left corner. It may be concluded that the appearance of the vortex ring is dependent on the Reynolds number and forms itself late for lower Reynolds numbers. As the Reynolds number is an indicator for the turbulence, this will certainly make sense.

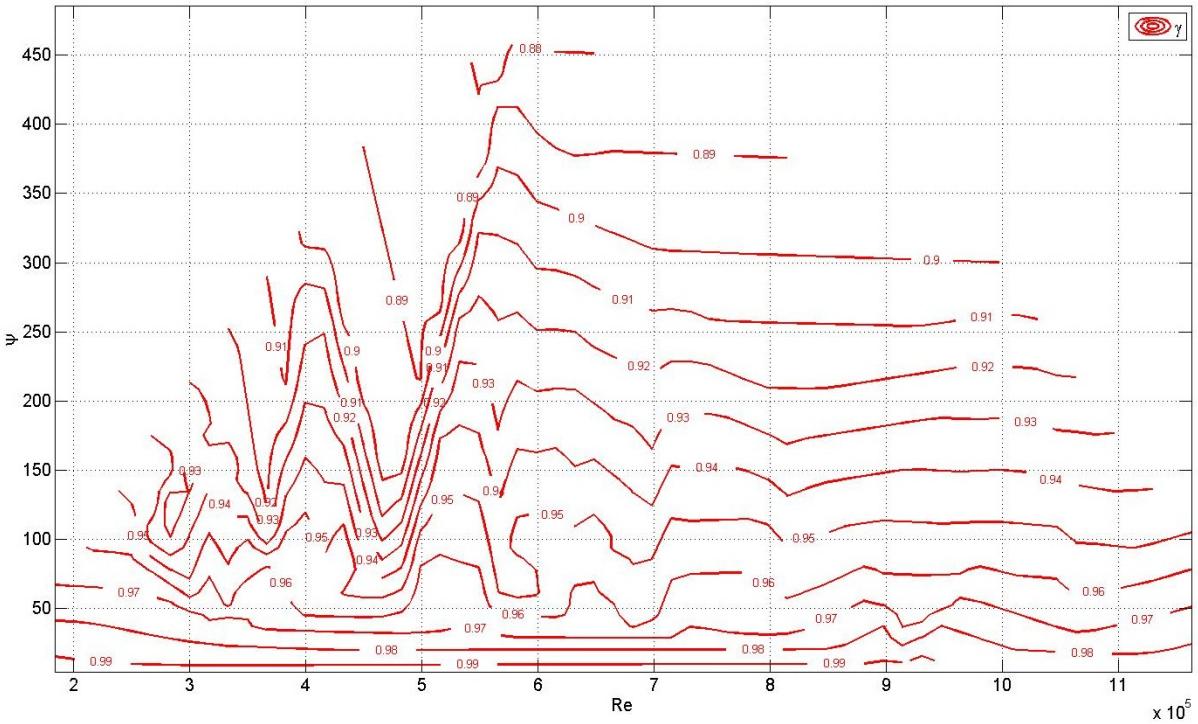

Figure 5-8 : contour line graph of the survey area

5.3 Design recommendations

As we have seen, low Ψ values which apparently lead to a good flow distribution can be achieved by small storage diameters, large diffuser heights and large inlet diameters. All these characteristics are economic disadvantages because they lead to a more expensive construction with a small storage volume in proportion to the housing.

Moreover the suggested design of the storage would be long and slim. This tube-shaped design will cause a negative impact on the pressure drop and would increase the attrition during charging and discharging. So it can be said that an increase of the efficiency of the possible storage capacity has to be offset by higher coasts of the construction and during operation. Hence, the dimensions of the storage must be weighted to achieve a cheap storage with a good performance. It might be argued that a local optimum would be a design which just do not lead to the formation of a vortex ring but the global optimum may be found somewhere else.

6 Summary and Outlook

All aims which were described in the introduction could be achieved. Much effort has been expended for the mesh independence study, but it was worth it. In fact the mesh is a bit finer than needed but this made it possible to attain exact results for the investigation of a wide survey area with the tool of automated mesh generation.
Another important point of this study is the completed verification of the Ψ-Re correlation. This approach is generally interesting for the dimensioning of the flow distributors of heat storages. The conclusions which can be drawn from this correlation and the resulting diagrams can make significant predictions for the dimensioning of sensible heat storages using packed beds.
The results may be interpreted as follows: It could be identified a significant influence of the geometry of the flow distributor on the flow distribution. However, the simulation results indicate that the inlet mass flow rate, the velocity and the temperature which had been summed up to the Reynolds number, do not have so much influence on the flow distribution. Nonetheless, these parameters which can be combined to the Reynolds number cause the non-linearity observed in Figure 5-7. This perception should be checked and considered for part load charging of sensible heat storages with the investigated dimension range.
Therefore the aim of finding the most influencing parameters was achieved. The storage and the inlet diameter are the significant parameters for the flow distribution. The results even suggest a maximal value for the inlet diameter or for the diameter quotient of a frustoconical flow distributor which should be investigated in future research.
Nevertheless, as there is no possibility for verification of the simulation results this should be done before considering as true. Usually the simulation model can be improved with experimental data of a existing set-up in a iterative procedure; results without this step should not be used for applications. Consequently some expensive experiments are necessary to check the significance of the presented results, in particular the predicted minimum should be investigated because its prognosis leads to restrictions of the design margin of frustoconical flow distributors.
In order to pursue the research in this area, a similar study for the discharging process should be done. Further, the behavior of the real storage capacity for different Gamma values should be investigated, to check, if the assumption that high Gamma values lead to an effective use of the storage is really appropriate.
Another interesting research area would be the investigation of an optimal storage geometry considering economical factors to find the geometry with the best cost-performance ratio.

7 Bibliography

[1] Ali H. Abedin and Marc A. Rosen, A Critical Review of Thermochemical Energy Storage Systems, The Open Renewable Energy Journal, 2011, 4, 42-46

[2] Van Berkel J. Storage of solar energy in chemical reactions. In: Jean-Christophe Hadorn, editor. Thermal energy storage for solar and low energy buildings. Spain: Lleida; 2005.

[3] Boussinesq, J. (1877): Théorie de l'écoulement tourbillant.

[4] Coutier JP, Faber EA. Two applications of a numerical approach of heat transfer process within rock beds. Solar Energy 1982;29(6):451–62.

[5] T J Craft, S E Grant, A V Gerasimov, H Iacovides, B E Launder, Wall Function Strategies for Use in Turbulent Flows,

[6] Dincer I, Rosen MA. Thermal energy storage, systems and applications. New York: Wiley; 2002.

[7] Do Couto Aktay KS, Tamme R, Müller-Steinhagen H. Thermal conductivity of high-temperature multicomponent materials with phase change. Int J Thermophys 2008;29:678–92.

[8] R. Eymard, T Gallouët and R. Herbin, update of the article published in Handbook of Numerical Analysis, 2000

[9] Foster M. Theoretical investigation of the system SnOx/Sn for the thermochemical storage of solar energy. In: Proceedings of the 11th SolarPACES. International Symposium on Concentrated Solar Power and Chemical Energy Technologies; 2002.

[10] Ferziger, Joel ; Peric, Milovan: Numerische Strömungsmechanik. Berlin Heidelberg : Springer, 2008

[11] FLUENT Theory Guide

[12] FLUENT User Guide

[13] Antoni Gil, Marc Medrano, Ingrid Martorell, Ana La´zaro, Pablo Dolado, Bele´n Zalba, Luisa F. Cabeza, State of the art on high temperature thermal energy storage for power generation. Part 1—Concepts, materials and modellization Renewable and Sustainable Energy Reviews 14 (2010) 31–55

[14] Hahn Joachim, Evaluierung eines Tropfenmodells für turbulente Strömungen. 2009

[15] Markus Hänchen, Sarah Brückner, Aldo Steinfeld; High-temperature thermal storage using a packed bed of rocks e Heat transfer analysis and experimental validation, Applied Thermal Engineering 31 (2011) 1798-1806

[16] Hansen M.: „Strömungsvorgänge im Cowper“, abgedruckt in Hundert Jahre

Cowper-Winderhitzung, Brohltal A.-G. für Stein- und Tonindustrie, Burgbrohl 1958

[17] Harmeet Singh, R.P. Saini , J.S. Saini, A review on packed bed solar energy storage systems, Renewable and Sustainable Energy Reviews 14 (2010) 1059–1069

[18] Hasnain SM. Review on sustainable thermal energy storage technologies, part I: heat storage materials and techniques. Energy Convers Manage 1998;39: 1127–38.

[19] M. Hölling, H. Herwig. CFD-TODAY: Anmerkungen zum kritischen Umgang mit kommerziellen Software-Programmpaketen. Forschung im Ingenieurwesen 68 (2004) 150–154

[20] Institut für Wärmetechnik TU Graz, Sonnenenergienutzung, Grundlagen der Sonnenenergieeinstrahlung (05-10)

[21] IPCC Fourth Assessment Report: Climate Change (2007), Synthesis Report, http://www.ipcc.ch/publications_and_data/ar4/syr/en/main.html

[22] K.A.R. Ismail , R. Stuginsky Jr.(1999): A parametric study on possible fixed bed models for pcm and sensible heat storage, Applied Thermal Engineering 19 757-788

[23] Murat Kenisarin, Khamid Mahkamov, Solar energy storage using phase change materials, Renewable and Sustainable Energy Reviews, Volume 11, Issue 9, December 2007, Pages 1913–1965

[24] Krauter R, (2006) Mikroporöse Materialen speichern verlustfrei Wärmeenergie über Monate, Deutschlandfunk, http://www.dradio.de/dlf/sendungen/forschak/505994/

[25] D. Laing, D. Lehmann, M. Fiss, C. Bahl, Test results of concrete thermal energy storage for parabolic trough power plants, ASME J. Sol. Energ. Eng. 131 (4) (2009) 041007.

[26] Lane GA. Solar heat storage: latent heat material, volume II: technology. CRC Press; 1986

[27] B. E. Launder and D. B. Spalding."The Numerical Computation of Turbulent Flow". Computer Methods in Applied Mechanics and Engineering. 3. 269–289. 1974.

[28] Stefan Lecheler, Numerische Strömungsberechnung, Vieweg + Teubner Verlag/ Springer Fachmedien Wiesbaden GmbH, 2011

[29] Manuel Lier, 2008, Strömungssimulation der Gasverteilung im Ein- und Auslassbereich eines Hochtemperatur-Wärmespeichers

[30] National Renewable Energy Laboratory, (2010) Parabolic Through Thermal Energy Storage,

http://www.nrel.gov/csp/troughnet/thermal_energy_storage.html

[31] Herbert Oertel jr., Martin Böhle, Strömungsmechanik, Friedr. Vieweg & Sohn Verlags/GWV Fachverlage GmbH, Wiesbaden, 2004.

[32] RWE Power, ADELE – Adiabatic compressed-air energy storage for electricity supply

[33] Michael Schäfer, Numerik im Maschinenbau, Springer Berlin Heidelberg, 1999

[34] Nicolas Schmidt, Thermodynamische und strömungsmechanische Untersuchung eines direkt durchströmten Hochtemperatur-Wärmespeichers für Solarturmkraftwerke. 2009

[35] Sharma Atul, Tyagi VV, Chen CR, Buddhi D. Review on thermal energy storage with phase change materials and applications. Renew Sust Energy Rev 2009;13(2):318–45.

[36] Spinnler, Seifert (2010) Solar Engineering, Vorlesungsunterlagen

[37] Tamme R, Laing D, Steinmann WD, Zunft S. Innovative thermal energy storage technology for parabolic trough concentration solar power plants. In: Proceedings EuroSun 2002, the 4th ISES Europe Solar Congress; 2002.

[38] Tamme, R. The DISTOR Project. Consortium–objective–achievements. DISTOR dissemination workshop. Energy storage for direct steam solar power plants. Almeria, Spain; 2007.

[39] Tamme R. Concrete storage: update on the German concrete TES program. In: Workshop on thermal storage for trough power systems; 2003.

[40] Wilcox, David C. (1994): Turbulence Modeling for CFD. DCW Industries Inc. La Canada.

[41] W. E. Wentworth and E. Chen, Simple thermal decomposition reactions for storage of solar thermal energy, Solar Energy, Vol. 18. pp. 205-214. (1975)

8 Appendix

```
#Skript zur Netzgenerierung und Rechnungsinitialisierung mit Varaitionsparametern

$name="Basispunkt"                                          #Name der ausgegebenen Dateien
$pfad="D:/Geovariation/ceteris_paribus/Basispunkt"                  #root-Pfad
$mesh=$name+".msh"

#Anzahl der Knoten
$pipe=89                                                    #Anzahl horizontal Einlauf/Auslauf      89
$diffusor=481                                               #Anzahl horizontal Diffusoren           797
$center=433                                                 #Anzahl horizontal poröses Medium       433
$grenz=15                                                   #Anzahl vertikal Grenzschicht           11/16
$vertical=336                                               #Anzahl vertikal                        357

#Variationsparameter
        #Netz
        $h_v=5.3333                                             #Höhe des Diffusors
        $D=16/2                                                 #Radius des Speicherbetts
        $r_in=3/2                                               #Einlassrohrradius
        $H=$D                                                   #halbe Höhe des Speicherbetts

        #Berechnungsparameter
        $m=65.5635                                              #Einlassmassenfluss
        $T=923.15                                               #Einlasstemperatur

        #Übergabederivate
        $a=$H+$h_v
        $b=$H+$h_v+2
        $d_in=$r_in*2
        $HyD=$D*2

#Dicke Grenzschicht                                         #Nummern siehe Excel-Sheet
$c1=0.04
$c2=0.04
$c3=0.22
$c4=0.26

#Dicke Spacing
$s1=0.002
$s2=0.002
$s3=0.013
$s4=0.0172

new-item standard.rpl -type file                                    #erstellen des replay-Files
new-item initialisierung.jou -type file                             #erstellen des journal-Files

#Code für die Geometrieerstellung
"ic_geo_new_family GEOM" | Add-content standard.rpl
"ic_boco_set_part_color GEOM" | Add-content standard.rpl
"ic_empty_tetin" | Add-content standard.rpl
"ic_point {} GEOM pnt.00 0,0,0" | Add-content standard.rpl
```

"ic_point {} GEOM pnt.01 $H,0,0" | Add-content standard.rpl
"ic_point {} GEOM pnt.02 $a,0,0" | Add-content standard.rpl
"ic_point {} GEOM pnt.03 $b,0,0" | Add-content standard.rpl
"ic_point {} GEOM pnt.04 $b,$r_in,0" | Add-content standard.rpl
"ic_point {} GEOM pnt.05 $a,$r_in,0" | Add-content standard.rpl
"ic_point {} GEOM pnt.06 $H,$D,0" | Add-content standard.rpl
"ic_point {} GEOM pnt.07 0,$D,0" | Add-content standard.rpl
"ic_gui_set va_set(name)" | Add-content standard.rpl
"ic_delete_geometry curve names crv.00 0" | Add-content standard.rpl
.
.
.

#Erstellung des FLUENT-journals

"file/read-case $([char]34)$mesh$([char]34)" | Add-content initialisierung.jou
"define/models/axisymmetric yes" | Add-content initialisierung.jou
"grid/scale 1 1" | Add-content initialisierung.jou
"mesh/check" | Add-content initialisierung.jou
"define/models/energy yes no no no yes" | Add-content initialisierung.jou
"define/models/viscous/ke-standard yes" | Add-content initialisierung.jou
"define/operating-conditions/operating-pressure 100000" | Add-content initialisierung.jou
"define/operating-conditions/gravity yes -9.81 0" | Add-content initialisierung.jou
.
.
.

Erklärung:
Hiermit versichere ich, die vorliegende Arbeit selbstständig verfasst zu haben. Ich habe keine anderen Quellen und Hilfsmittel als die angegebenen verwendet.

Ort, Datum

Unterschrift